

Fast and Distributed Equivariant Graph Neural Networks by Virtual Node Learning

Yuelin Zhang^{*123}, Jiacheng Cen^{*123}, Jiaqi Han⁴, Wenbing Huang^{✉123}

Abstract—Equivariant Graph Neural Networks (GNNs) have achieved remarkable success across diverse scientific applications. However, existing approaches face critical efficiency challenges when scaling to large geometric graphs and suffer significant performance degradation when the input graphs are sparsified for computational tractability. To address these limitations, we introduce FastEGNN and DistEGNN, two novel enhancements to equivariant GNNs for large-scale geometric graphs. FastEGNN employs a key innovation: a small ordered set of virtual nodes that effectively approximates the large unordered graph of real nodes. Specifically, we implement distinct message passing and aggregation mechanisms for different virtual nodes to ensure mutual distinctiveness, and minimize Maximum Mean Discrepancy (MMD) between virtual and real coordinates to achieve global distributedness. This design enables FastEGNN to maintain high accuracy while efficiently processing large-scale sparse graphs. For extremely large-scale geometric graphs, we present DistEGNN, a distributed extension where virtual nodes act as global bridges between subgraphs in different devices, maintaining consistency while dramatically reducing memory and computational overhead. We comprehensively evaluate our models across four challenging domains: N-body systems (100 nodes), protein dynamics (800 nodes), Water-3D (8,000 nodes), and our new Fluid113K benchmark (113,000 nodes). Results demonstrate superior efficiency and performance, establishing new capabilities in large-scale equivariant graph learning. Code is available at <https://github.com/GLAD-RUC/DistEGNN>.

Index Terms—Graph Neural Networks, Equivariance, Geometric Graphs, Virtual Nodes, Efficiency.

I. INTRODUCTION

VARIOUS scientific data, such as chemical molecules, proteins, and particle-based physical systems, are often represented as geometric graphs [1]. Unlike standard graph representations, geometric graphs additionally assign each node a set of geometric vectors—for example, 3D atomic coordinates in molecules. These graphs exhibit prominent symmetries, including translations, rotations, and reflections, stemming from

* denotes equal contributions; ✉ denotes the corresponding author: hwenbing@ruc.edu.cn.

¹ Gaoling School of Artificial Intelligence, Renmin University of China, Beijing 100872, China.

² Beijing Key Laboratory of Research on Large Models and Intelligent Governance, Beijing 100872, China.

³ Engineering Research Center of Next-Generation Intelligent Search and Recommendation, MOE, Beijing 100872, China.

⁴ Department of Computer Science, Stanford University, CA 94305, USA.

This work has been submitted to the IEEE for possible publication. Copyright may be transferred without notice, after which this version may no longer be accessible.

the invariance of physical laws governing atomic (or particle) dynamics under changes in absolute position and orientation. When modeling such data, it is essential to incorporate these symmetries into the design, leading to the development of equivariant Graph Neural Networks (GNNs) [2, 3, 4]. In recent years, equivariant GNNs have achieved remarkable success in scientific applications, including physical dynamics simulation [5, 6], protein generation [7, 8], and many others.

Despite significant progress, existing equivariant GNNs face efficiency challenges when handling large geometric graphs, which are common in physical dynamics simulations. For example, EGNN [9], one of the most widely used models, incurs quadratic complexity in message exchange for fully connected graphs, making it impractical for large-scale scenarios like fluid dynamics simulations, where particle counts often exceed tens of thousands. A straightforward solution to improve efficiency is to reduce the number of edges, such as by restricting message passing to local neighbors within a cutoff radius. However, this approach risks losing long-range interactions and may degrade model performance.

In this paper, we address the aforementioned challenge by introducing *virtual nodes*. For clarity, we refer to the original nodes in geometric graphs as *real nodes*. Each virtual node is designed to connect to all real nodes as well as other virtual nodes, enabling dense, global message passing. This preserves expressive power even when the underlying geometric graph is sparsified for efficiency. Drawing inspiration from the physics principle of equivalent particle interactions [10], we propose learning virtual nodes that serve as compact, representative proxies for groups of real nodes. To ensure effectiveness, these virtual nodes must satisfy two key geometric properties: *Mutual distinctiveness* encoding diverse structural features of the graph, and *Global distributedness* maintaining spatial alignment with the real nodes’ distribution. These properties are interdependent and fundamental to the success of our method.

Specifically, we propose two efficient geometric GNN variants based on EGNN [9]: FastEGNN and DistEGNN¹. In FastEGNN, we introduce an ordered set of virtual nodes, where each node assumes a distinct semantic role and undergoes independent message passing. This architecture explicitly enhances mutual distinctiveness among virtual nodes. Furthermore, we employ Maximum Mean Discrepancy (MMD) [12] with an E(3)-invariant kernel to optimize the spatial alignment between virtual and real node coordinates, thereby improving global distributedness. Together, these innovations enable FastEGNN

¹This work is an extension of our previous conference version [11].

to efficiently simulate sparse graphs on a single device (*e.g.*, GPU) without compromising performance.

To handle extremely large graphs (*e.g.*, those exceeding 100K nodes) that surpass single-device capacity, we propose DistEGNN, a distributed extension of FastEGNN designed for multi-device parallel execution. Our approach employs a graph partitioning strategy to decompose the large graph into smaller subgraphs, which are distributed across multiple computing devices for parallel processing. While this partitioning improves scalability, it inherently introduces information loss across subgraph boundaries. To mitigate this, we implement a shared set of virtual nodes that span all devices, with their states continuously synchronized during training. This design serves two critical purposes: 1. Enabling global context propagation throughout the entire graph; 2. Facilitating cross-subgraph information fusion. By maintaining these global connections, DistEGNN effectively preserves the structural integrity of the complete graph while achieving efficient distributed computation, thereby minimizing the performance degradation typically associated with partitioned graph processing.

To sum up, our main contributions are as follows.

- We propose FastEGNN upon EGNN [9], which introduces learnable virtual nodes to enable efficient global message passing on sparse large geometric graphs. By explicitly optimizing virtual nodes for mutual distinctiveness and global distributedness, our method preserves expressive power while maintaining computational efficiency. Moreover, we consider virtual node learning as a general plug-in and extend it to more backbones, including RF, SchNet, and TFN.
- We further propose DistEGNN, a distributed extension of FastEGNN that breaks the memory barrier of single-device processing through innovative graph partitioning and synchronized virtual nodes learning. Our approach maintains model accuracy while enabling distributed processing of large-scale geometric graphs.
- We conduct comprehensive experiments to evaluate our proposed methods against State-Of-The-Art (SOTA) baselines across four challenging domains: N-body systems, Protein Dynamics, Water-3D, and our newly introduced Fluid113K dataset. To the best of our knowledge, this is the first work to perform equivariant graph learning on geometric graphs with over 100K nodes, significantly advancing the scalability frontier in this field. The results demonstrate both the efficiency and effectiveness of our models on such large-scale geometric graphs.

II. RELATED WORK

Geometric GNNs. Geometric GNNs can be classified into invariant and equivariant models. Invariant GNNs, exemplified by SchNet [13] and DimeNet [14], have made initial attempts to embed geometric information into invariance features like distance and angles. However, a notable gap still exists in achieving full equivariance within these models, leading to the study of equivariant GNNs. For example, high-degree steerable GNNs, including TFN [15], SEGNN [16], and SE(3)-Transformer [17], leverage the equivariance of spherical

harmonics, offering commendable physical interpretability. Nevertheless, the substantial computational cost associated with spherical harmonic forms poses a significant limitation for their application in large-scale tasks. In addition to the aforementioned models, scalarization-based GNNs [9, 18, 19, 20] present a more elegant and expedient approach to representing geometric information, relying solely on linear combinations of geometric vectors. Despite the rich literature and sophisticated architectures, the effectiveness of geometric GNNs usually relies on densely connected geometric graphs to ensure accuracy. However, this necessity introduces high complexity, thereby constraining the practical implementation of geometric GNNs in large-scale scientific problems. Our work tackles these challenges, aiming to enhance the scalability and applicability of geometric GNNs in scientific domains.

Virtual nodes for GNNs. In prior investigations on conventional GNNs [21, 22, 23], attempts were made to maintain graph connectivity by introducing virtual nodes connected to all graph nodes. This design ensures that any two nodes can exchange information through the process of reading from and writing into virtual nodes at each step of message passing. In the realm of geometric GNNs, certain existing approaches treat virtual nodes as specifically defined clusters based on prior knowledge. They are exclusively connected to nodes belonging to the same cluster, such as different objects in SGNN [24] or distinct protein chains in MEAN [25]. In contrast to these methods, our approach involves end-to-end learning of virtual nodes from the dataset, eliminating the reliance on prior or external knowledge. Notably, the learning process for virtual nodes is thoughtfully designed to ensure both mutual distinctiveness and global distributedness.

Scalability of GNNs. In the field of conventional GNNs, extensive efforts have been made to address the computational and memory bottlenecks of processing large-scale graphs. Early approaches primarily focused on designing sampling strategies, which reduce the overhead by performing message passing on a subset of sampled neighbors. These approaches are typically include node-level, layer-level, and graph-level sampling [26, 27]. Recently, DistGNN [28] proposed a distributed training framework for 2D graphs. To reduce cross-device communication costs, it integrates many complex algorithms, such as minimal vertex partitioning, shared memory, and delayed updates. However, this also increases the difficulty of implementation and deployment. Different from above methods, our DistEGNN is the first distributed framework specifically designed for geometric graphs with 3D spatial structures. We carefully design the distributed message passing formula to preserve E(3)-equivariance. Furthermore, we leverage a set of shared, ordered virtual nodes to effectively propagate global information. This significantly speeds up the training process while maintaining remarkable predictive accuracy.

III. PRELIMINARIES

Geometric graph. A geometric graph of N nodes is defined as $\vec{\mathcal{G}} := (\vec{X}, \mathbf{H}; \mathcal{E})$, where $\vec{X} = [\vec{x}_1, \vec{x}_2, \dots, \vec{x}_N]^\top \in \mathbb{R}^{N \times 3}$ is the collection of 3D coordinates for the nodes, $\mathbf{H} = [\mathbf{h}_1, \mathbf{h}_2, \dots, \mathbf{h}_N]^\top \in \mathbb{R}^{N \times H}$ is the node feature

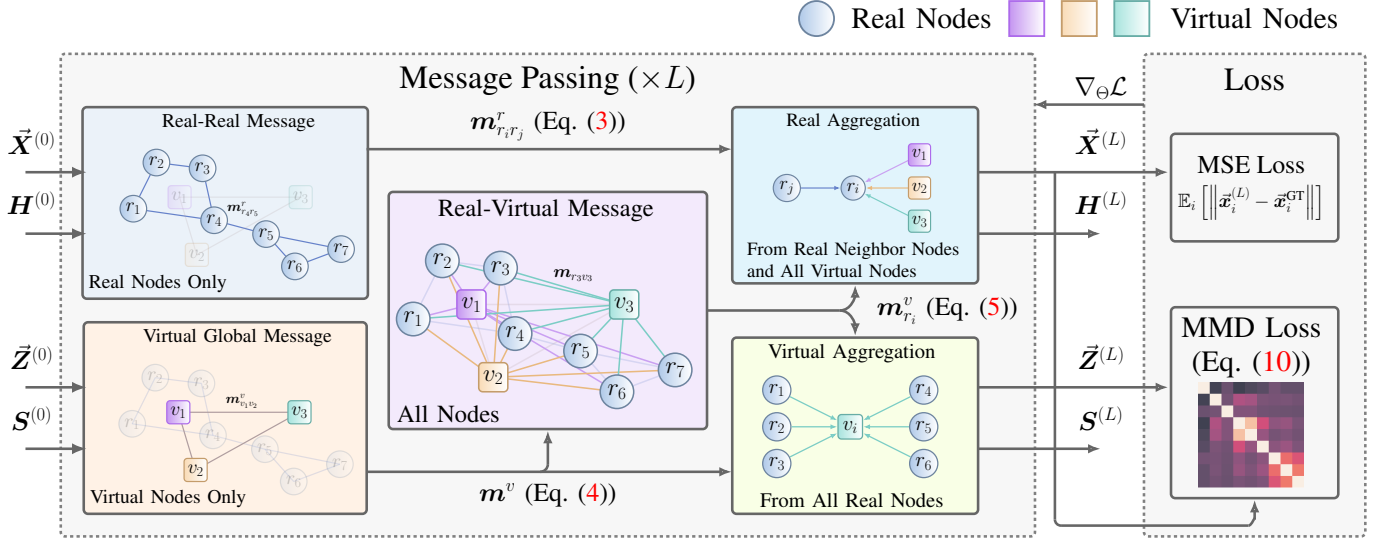


Fig. 1. The overall architecture of FastEGNN. (\vec{X}, H) are the real coordinates and features; (\vec{Z}, S) are the virtual coordinates and features. Each layer contains 5 components: Real-Real Message $m_{r_i r_j}^r$, Virtual Global Message m^v , Real-Virtual Message $m_{r_i}^v$, Real Aggregation, and Virtual Aggregation. The real-real and real-virtual edges are displayed with different colors to indicate that the message passing and aggregation functions over the edges are different.

matrix, and \mathcal{E} is the set of edges representing the interactions between nodes. In the physical dynamics simulation scenarios, we are additionally provided with the velocities $\vec{V} = [\vec{v}_1, \vec{v}_2, \dots, \vec{v}_N]^\top \in \mathbb{R}^{N \times 3}$ and optionally the edge feature $e_{ij} \in \mathbb{R}^E$ for every edge $(i, j) \in \mathcal{E}$.

Equivariance. Formally, a function ϕ is equivariant *w.r.t.* group G if $\phi(\rho_X(g)\mathbf{x}) = \rho_Y(g)\phi(\mathbf{x})$, $\forall g \in G$, where $\rho_X(g)$ and $\rho_Y(g)$ are the representation of transformation g in the input space \mathcal{X} and output space \mathcal{Y} , respectively. In this work, we focus on the 3D Euclidean group $E(3)$, whose elements $g \in E(3)$ can be realized by an orthogonal matrix $O \in \mathbb{R}^3$, $O^\top O = I$ and a translation vector $\vec{t} \in \mathbb{R}^3$. By this means, every $E(3)$ -equivariant GNN ϕ on geometric graph $\vec{\mathcal{G}}$ taking as input coordinates \vec{X} , velocities \vec{V} , and node features H should satisfy the following constraint for all $(O, \vec{t}) \in E(3)$:

$$\vec{X}'O + \vec{t}, H' = \phi(\vec{X}O + \vec{t}, \vec{V}O, H, \mathcal{E}), \quad (1)$$

where $\vec{X}', H' = \phi(\vec{X}, \vec{V}, H, \mathcal{E})$ are the updated coordinates and node features. Note that the velocities \vec{V} are not affected by the translation \vec{t} . We do not specify permutation equivariance in Eq. (1), since it has been intrinsically encoded in GNNs.

Problem formulation. We mainly focus on the position prediction task which is fundamental to many physical simulation scenarios [17, 9]. Specifically, given the initial geometric graph with coordinates \vec{X} , node features H , velocities \vec{V} , edges \mathcal{E} and their attributes $\{e_{ij} : (i, j) \in \mathcal{E}\}$, we seek to predict \vec{X}' as the positions after a fixed time Δt . It is an $E(3)$ -equivariant task, since if we rotate or translate the initial positions, the predicted positions should rotate or translate in accordance. That is, we aim to design an $E(3)$ -equivariant function ϕ that meet the constraint of Eq. (1).

IV. FASTEGNN

In this section, we introduce the details of our proposed FastEGNN. We first present the representation of virtual nodes

in Section IV-A. Then, we design the message passing and aggregation among the real and virtual nodes in Section IV-B, and provide the learning objectives of our model in Section IV-C. Finally, we will explain the benefit of involving virtual nodes in large geometric graph learning in Section IV-D.

As claimed in Introduction, FastEGNN is designed to ensure the mutual distinctiveness and the global distributedness of the virtual nodes. We will specify that the mutual distinctiveness is guaranteed by the independent parameterization of the virtual nodes in Section IV-A, and separate message passing and aggregation with different functions in Section IV-B. As for the global distributedness, we achieve this property by employing the MMD loss as a regularization term in Section IV-C.

A. Geometric graphs with virtual nodes

With the input geometric graph $\vec{\mathcal{G}}$ as defined before, we create an augmented geometric graph $\vec{\mathcal{G}}^v$ by adding a set of C virtual nodes (\vec{Z}, S) , where $\vec{Z} \in \mathbb{R}^{3 \times C}$ and $S \in \mathbb{R}^{H \times C}$ refer to the 3D coordinates and invariant features, respectively. Each virtual node is connected to all real nodes in $\vec{\mathcal{G}}$, as well as each other virtual node. This augments the original edge set \mathcal{E} with new connections, leading to \mathcal{E}^v . Overall, $\vec{\mathcal{G}}^v := (\vec{X}, \vec{V}, H; \vec{Z}, S; \mathcal{E}^v)$.

As the virtual nodes are not observed in the input data, we need to handcraft the initialization of their values. We adopt the following initialization strategy for the virtual nodes: $\vec{Z} = \frac{1}{N} \sum_{i=1}^N \vec{x}_i \mathbf{1}^\top$, where each channel in \vec{Z} is initialized as the Center-of-Mass (CoM) of the input geometric graph, ensuring $E(3)$ -equivariance; each channel of $S \in \mathbb{R}^{H \times C}$ is initialized as independent learnable parameters that are optimized during training. In form, the virtual nodes are initialized as a function of the real nodes, namely, $\vec{Z}, S = \varphi_{\text{init}}(\vec{X}, H)$, which should abide by:

$$O\vec{Z} + \vec{t}, S = \varphi_{\text{init}}(P\vec{X}O + \vec{t}, PH), \quad (2)$$

for any orthogonal transformation $\mathbf{O} \in \mathbb{R}^{3 \times 3}$, translation $\vec{t} \in \mathbb{R}^3$, and permutation $\mathbf{P} \in \{0, 1\}^{N \times N}$. $\vec{\mathbf{Z}}$ is E(3)-equivariant and permutation-invariant with respect to $\vec{\mathbf{X}}$.

One crucial point we would like to emphasize is that the channels of $\vec{\mathbf{Z}}$ (and \mathbf{S}) actually form an *ordered* set; in other words, different channel, namely, different virtual node, is endowed with different meaning and can not be organized in arbitrary permutation. This restriction, along with the separate message passing mechanism in the next subsection, serves our purpose of attaining the mutual distinctiveness amongst the virtual nodes. Besides, such orderliness also facilitates the derivation of the message function with universal expressivity, which will be detailed in Section IV-D.

B. Message Passing and Aggregation

After obtaining the initialized virtual nodes, we conduct the update of all virtual nodes and all real nodes via E(3)-equivariant message passing, as illustrated in Fig. 1. This includes real-real message computation, virtual global message calculation, real-virtual message derivation, real node aggregation, and virtual node aggregation. We introduce each component in detail below.

We denote by $(\vec{\mathbf{X}}^{(0)}, \vec{\mathbf{V}}^{(0)}, \mathbf{H}^{(0)}; \vec{\mathbf{Z}}^{(0)}, \mathbf{S}^{(0)}; \mathcal{E}^v)$ the initialization, and specify the l -th layer with superscript l .

Real-Real message. We first derive the message between all the real nodes in the way akin to EGNN [9], which is given by:

$$\mathbf{m}_{ij}^r = \varphi_1(\mathbf{h}_i^{(l)}, \mathbf{h}_j^{(l)}, \|\vec{\mathbf{x}}_i^{(l)} - \vec{\mathbf{x}}_j^{(l)}\|^2, \mathbf{e}_{ij}), \quad (3)$$

where φ_1 is a Multi-Layer Perceptron (MLP).

Virtual global message. Distinct virtual node represents distinct aspect of the geometric graph. Therefore, exhausting the correlation between each pair of the virtual nodes is able to reflect the entire behavior of the input system. To do so, we compute an invariant matrix extracted from the inner-product of the center-translated virtual coordinates:

$$\mathbf{m}^v = (\vec{\mathbf{Z}}^{(l)} - \bar{\mathbf{x}}\mathbf{1}^\top)^\top (\vec{\mathbf{Z}}^{(l)} - \bar{\mathbf{x}}\mathbf{1}^\top), \quad (4)$$

where $\bar{\mathbf{x}} = \frac{1}{N} \sum_{i=1}^N \vec{\mathbf{x}}_i$ is the CoM of the geometric graph. Clearly, $\mathbf{m}^v \in \mathbb{R}^{\bar{C} \times \bar{C}}$ is an E(3)-invariant matrix, and indeed an universal approximation of any E(3)-invariant function of the virtual coordinates $\vec{\mathbf{Z}}^{(l)}$, according to the proof of Lemma 2 in [29].

Real-Virtual message. The next step is to compute the message between the real nodes and the virtual nodes by:

$$\mathbf{m}_i^v = \varphi_2 \left(\mathbf{h}_i^{(l)}, \mathbf{S}^{(l)}, \bigoplus_{c=1}^C \|\vec{\mathbf{x}}_i^{(l)} - \vec{\mathbf{z}}_c^{(l)}\|^2, \mathbf{m}^v \right), \quad (5)$$

where \bigoplus defines the concatenations along the channel dimension, and φ_2 is an MLP. Eq. (5) returns the message between each real node i and the global virtual set, which will be consistently applied during the later real and virtual node aggregation processes. Again, Eq. (5) is E(3)-invariant. In our implementation, we find that computing message between real node i and virtual node c separately, namely, $\mathbf{m}_{ic}^v = \varphi_2 \left(\mathbf{h}_i^{(l)}, \mathbf{s}_c^{(l)}, \|\vec{\mathbf{x}}_i^{(l)} - \vec{\mathbf{z}}_c^{(l)}\|^2, \mathbf{m}_c^v \right)$ enables more effective training and better performance, in contrast to the global

message from all virtual nodes in Eq. (5). Here, \mathbf{m}_c^v denotes the c -th column of \mathbf{m}^v .

Real aggregation. Given the real-real message \mathbf{m}_{ij}^r and real-virtual message \mathbf{m}_i^v , we are ready to derive the message aggregation for real node i as follows:

$$\begin{aligned} \vec{\mathbf{x}}_i^{(l+1)} &= \vec{\mathbf{x}}_i^{(l)} + \alpha_i \sum_{j \in \mathcal{N}(i)} (\vec{\mathbf{x}}_i^{(l)} - \vec{\mathbf{x}}_j^{(l)}) \varphi_x^r(\mathbf{m}_{ij}^r) + \\ &\quad \frac{1}{C} \sum_{c=1}^C (\vec{\mathbf{x}}_i^{(l)} - \vec{\mathbf{z}}_c^{(l)}) \varphi_x^v(\mathbf{m}_{ic}^v) + \varphi_v(\mathbf{h}_i^{(l)}) \vec{\mathbf{v}}_i^{(0)}, \quad (6) \\ \mathbf{h}_i^{(l+1)} &= \mathbf{h}_i^{(l)} + \varphi_h \left(\mathbf{h}_i^{(l)}, \alpha_i \sum_{j \in \mathcal{N}(i)} \mathbf{m}_{ij}^r, \bigoplus_{c=1}^C \mathbf{m}_{ic}^v \right), \quad (7) \end{aligned}$$

where $\alpha_i = \frac{1}{|\mathcal{N}(i)|}$, $\varphi_x^r, \varphi_x^v, \varphi_v$ are MLPs outputting one-dimensional scalars, and φ_h is also an MLP with the output dimension complying with that of $\mathbf{h}_i^{(l+1)}$. The update of $\vec{\mathbf{x}}_i^{(l+1)}$ (and similarly $\mathbf{h}_i^{(l+1)}$) is inspired by EGNN but further extended with the message from the virtual nodes, namely, the term $\sum_{c=1}^C (\vec{\mathbf{x}}_i^{(l)} - \vec{\mathbf{z}}_c^{(l)}) \varphi_x^v(\mathbf{m}_{ic}^v)$. Previous idea of adding a global node in SGNN [24] is more like a degenerated version of Eq. (6) where φ_x^r and φ_x^v are shared. It is important to note that as the number of channels C increases, the concatenation form $\bigoplus_{c=1}^C \mathbf{m}_{ic}^v \in \mathbb{R}^{CH}$ in Eq. (7) results in a significant increase in the number of MLP parameters. To enhance the scalability, we instead adopt the summation form $\beta \sum_{c=1}^C \mathbf{m}_{ic}^v$, where $\beta = \frac{1}{C}$.

Virtual aggregation. Now, we devise the virtual node aggregation as:

$$\vec{\mathbf{z}}_c^{(l+1)} = \vec{\mathbf{z}}_c^{(l)} + \frac{1}{N} \sum_{i=1}^N (\vec{\mathbf{z}}_c^{(l)} - \vec{\mathbf{x}}_i^{(l)}) \varphi_Z(\mathbf{m}_{ic}^v), \quad (8)$$

$$\mathbf{s}_c^{(l+1)} = \mathbf{s}_c^{(l)} + \varphi_S \left(\mathbf{s}_c^{(l)}, \frac{1}{N} \sum_{i=1}^N \mathbf{m}_{ic}^v \right), \quad (9)$$

where, $\varphi_Z \in \mathbb{R}$ and φ_S are also MLPs. To be specific, the calculation $\sum_{i=1}^N (\vec{\mathbf{z}}_c^{(l)} - \vec{\mathbf{x}}_i^{(l)}) \varphi_Z(\mathbf{m}_{ic}^v)$ in Eq. (8) aggregates all messages from all real nodes, multiplied with different scalar $\varphi_Z(\mathbf{m}_{ic}^v)$. In this way, the update of different virtual node is independent to each other, for the sake of encouraging better mutual distinctiveness.

We have the flowing theoretical assurance by our design:

Proposition IV.1. *If the initialization of the virtual nodes satisfies Eq. (2), then after Eqs. (3) to (9), the output coordinates $\vec{\mathbf{X}}^{(L)}$ are E(3)-equivariant and permutation-equivariant, the virtual coordinates $\vec{\mathbf{Z}}^{(L)}$ are E(3)-equivariant and permutation-invariant, with respect to the input $\vec{\mathbf{X}}^{(0)}$.*

C. Learning Objectives

In this subsection, we exploit the MMD objective [12] to enforce the alignment between virtual and real coordinates. MMD is widely used in the research of domain adaption. Here, we derive \mathcal{L}_{MMD} without the original term $k(\vec{\mathbf{x}}_i^{(L)}, \vec{\mathbf{x}}_j^{(L)})$ as:

$$\frac{1}{C^2} \sum_{i=1}^C \sum_{j=1}^C k(\vec{\mathbf{z}}_i^{(L)}, \vec{\mathbf{z}}_j^{(L)}) - \frac{1}{NC} \sum_{i=1}^N \sum_{j=1}^C k(\vec{\mathbf{x}}_i^{(L)}, \vec{\mathbf{z}}_j^{(L)}), \quad (10)$$

where the RBF kernel $k(\vec{x}, \vec{y}) = \exp(-\frac{\|\vec{x}-\vec{y}\|^2}{2\sigma^2})$ is E(3)-invariant, hence the MMD loss is also E(3)-invariant. Interestingly, minimizing the first term in Eq. (10) is actually enlarging the divergence between the virtual nodes, while maximizing the second term enhances the similarity between the virtual nodes and the real ones. Note that we can just sample a small-scale subset of the real nodes for the MMD calculation at each iteration to avoid redundant costs. As the MMD is evaluated exclusively during training, this sampling strategy will not compromise the model's equivariance or invariance.

The overall training loss \mathcal{L} is a combination of the MSE loss between the predicted positions and the ground truth, together with the proposed auxiliary E(3)-invariant MMD loss to expand the coverage of the virtual nodes towards the data distribution:

$$\mathcal{L} = \mathcal{L}_{\text{MSE}}(\vec{X}^{(L)}, \vec{X}^{\text{GT}}) + \lambda \mathcal{L}_{\text{MMD}}(\vec{Z}^{(L)}, \vec{X}^{\text{GT}}), \quad (11)$$

where λ is the balancing factor between MSE and MMD.

D. Theoretical Analyses

The main complexity of FastEGNN lies in the aggregation processes for each node in Eqs. (6) and (7), where the number of the summation operations for all real nodes is $NK + NC$, with K denoting neighbor size. To improve the efficiency for large graphs, one solution is decreasing the value of K , which yet will diminish the interaction between the real nodes. In this subsection, we will explain that such diminution, owing to the involvement of the virtual nodes, is alleviated and our FastEGNN will still perform well even when K is decreased to zero, if the distribution of the virtual coordinates is well aligned with the real coordinates.

We focus on the update of the real coordinate \vec{x}_i by aggregating messages from its neighbors. Without loss of generality, we assume its neighbors to be the whole set \vec{X} . The update is denoted as the function $\vec{x}'_i = f(\vec{x}_i, \vec{X})$, which should be E(3)-equivariant *w.r.t.* the both inputs, and permutation-invariant *w.r.t.* \vec{X} . According to Proposition 10 in [30], we have the following result.

Proposition IV.2 ([30]). *The update function must take the form $f(\vec{x}_i, \vec{X}) = \vec{x}_i + \sum_{j=1}^N (\vec{x}_j - \vec{x}_i) \psi(\vec{x}_j - \vec{x}_i, \vec{x}_1 - \vec{x}_i, \dots, \vec{x}_{j-1} - \vec{x}_i, \vec{x}_{j+1} - \vec{x}_i, \dots, \vec{x}_N - \vec{x}_i)$, where $\psi : \mathbb{R}^{3N} \rightarrow \mathbb{R}$ is orthogonality-invariant, and permutation-invariant with respect to the last $N - 1$ inputs.*

While this result is theoretically elegant, it is not so practically helpful, since the universal form of ψ is still unknown. Existing equivariant GNNs (such as EGNN) only exploit its reduced but not sufficiently expressive version.

In our model, we need to aggregate the message from the virtual nodes \vec{Z} . The update function becomes $\vec{x}'_i = f(\vec{x}_i, \vec{Z})$. Notably, different from \vec{X} , the matrix \vec{Z} is an ordered set by our design, which entails that the permutation invariance of f is no longer required. This enables us to derive a more informative form of f as follows.

Proposition IV.3. *The update function must take the form $f(\vec{x}_i, \vec{Z}) = \vec{x}_i + \sum_{c=1}^C (\vec{z}_c - \vec{x}_i) \psi_c \left(\bigoplus_{c=1}^C \|\vec{z}_c - \vec{x}_i\|^2, \mathbf{m}^v \right)$, where $\psi_c : \mathbb{R}^{C+C^2} \rightarrow \mathbb{R}$ is an arbitrary non-linear function, and \mathbf{m}^v is an E(3)-invariant term by Eq. (5).*

The proof is based on Proposition 1 in SGNN [24], and provided in appendix. Proposition IV.3 is practically realizable by just implementing ψ_c via MLP, which is actually the form in our FastEGNN (Eq. (5)). More importantly, Proposition IV.3 suggests that $f(\vec{x}_i, \vec{Z})$ is able to universally approximate the messages from all the real nodes, if the virtual coordinates \vec{Z} can well approximate the real ones \vec{X} . As presented in the last subsection, we achieve this goal by penalizing the MMD loss. Our latter experiments will also support the theoretical analyses here, showing that FastEGNN with a small value of C can still perform promisingly even when all edges are dropped, while EGNN behaves poorly.

V. BESIDES FASTEGNN

Our proposed virtual node mechanism is designed to be modular, flexible, and easy to integrate. It can be applied to a variety of geometric graph neural networks as a plugin component, enabling performance improvements beyond the EGNN architecture. Specifically, the original network architecture remains unchanged, real nodes continue to exchange messages and update features according to the native rules of the baseline model. On top of this, we introduce an additional message pathway that allows real nodes to exchange information with virtual nodes. Since the virtual node interaction is implemented as an independent auxiliary module with its own learnable parameters and update rules, the mechanism can be easily plugged into various geometric graph neural network architectures without modifying the original model structure.

To examine its general applicability, we apply the mechanism to three representative geometric GNNs: RF [18], an equivariant model; SchNet [13], an invariant GNN; and TFN [15], a high-degree steerable model that leverages spherical harmonics for equivariant representation. In the following, we detail the coordinate update formulations used to implement each variant.

FastRF. RF is a scalarization-based equivariant model that shares a similar design with EGNN. However, it differs in that it computes messages solely based on node distances, without incorporating node features into message construction process. Accordingly, in implementing FastRF, we remove the node features \mathbf{h} from FastEGNN and also exclude the virtual node features \mathbf{S} to maintain consistency with RF's design.

FastSchNet. SchNet is an invariant geometric graph neural network. To update the spatial coordinates, we incorporate an equivariant coordinate prediction module that takes the invariant features generated by SchNet as input. Besides, real nodes receive additional messages from virtual nodes, and the overall update rule becomes:

$$\begin{aligned} \vec{x}_i^{(l+1)} = & \underbrace{\left[\vec{x}_i^{(l)} + \sum_{j \in \mathcal{N}_i} \varphi(\mathbf{h}_i^{(l)}, \mathbf{h}_j^{(l)}, \mathbf{e}_{ij})(\vec{x}_i^{(l)} - \vec{x}_j^{(l)}) \right]}_{\text{update by SchNet}} \quad (12) \\ & + \left[\frac{1}{C} \sum_{c=1}^C (\vec{x}_i^{(l)} - \vec{z}_c^{(l)}) \varphi_x^v(\mathbf{m}_{ic}^v) + \varphi_v(\mathbf{h}_i^{(l)}) \vec{v}_i^{(0)} \right]. \quad (13) \end{aligned}$$

FastTFN. Unlike the two models above, TFN is an SO(3)-equivariant model that leverages high-degree tensors and spher-

ical harmonics to model rotational symmetries. To implement FastTFN, we first reduce the number of the channels used in the original TFN to be 1, yielding single-channel TFN, which alleviates computational overhead and is found to be more compatible with virtual node learning. In each layer of FastTFN, the updated coordinates of real nodes are first computed using a TFN layer and then further refined by aggregating messages from virtual nodes via the following formulation:

$$\begin{aligned} \bar{\mathbf{x}}_i^{(l+1)} = & \underbrace{\left[\bar{\mathbf{x}}_i^{(l)} + \sum_{j \in \mathcal{N}_i} \mathbb{Y}^{\mathbb{L}} \left(\frac{\bar{\mathbf{x}}_i^{(l)} - \bar{\mathbf{x}}_j^{(l)}}{\|\bar{\mathbf{x}}_i^{(l)} - \bar{\mathbf{x}}_j^{(l)}\|} \right) \otimes_{\text{cg}}^{\mathbb{W}} \left(\mathbf{h}_j^{(l)} \|\bar{\mathbf{v}}_j^{(0)}\| \right) \right]}_{\text{update by TFN}} \\ & + \left[\frac{1}{C} \sum_{c=1}^C (\bar{\mathbf{x}}_i^{(l)} - \bar{\mathbf{z}}_c^{(l)}) \varphi_x^v(\mathbf{m}_{ic}^v) + \varphi_v(\mathbf{h}_i^{(l)}) \bar{\mathbf{v}}_i^{(0)} \right], \end{aligned} \quad (14)$$

$$(15)$$

where the $\bar{\mathbf{x}}_i^{(l)}$ is the coordinate of real node i , and $\mathbb{Y}^{\mathbb{L}}(\cdot)$ embeds the distance between real node i and j into spherical harmonics with type in set $\mathbb{L} = \{0, 1, 2, \dots, \text{max_degree}\}$. $\otimes_{\text{cg}}^{\mathbb{W}}(\cdot, \cdot)$ indicates Clebsch-Gordan (CG) tensor product with only type-1 outputs, the set \mathbb{W} contains the corresponding learnable weights [2], \mathbf{h}_j and $\bar{\mathbf{v}}_j$ are features (type-0) and velocity (type-1) of real node j respectively.

VI. DISTEGNN

Distributed training can significantly improve the scalability and computational efficiency of geometric GNNs. By distributing the data and computation overhead of large-scale geometric graphs across multiple devices, it not only accelerates the training process but also enables the model to handle extremely large graph structures that are otherwise infeasible on a single device. This capability is particularly important for simulating real-world systems with complex and mass spatial relationships.

Taking advantage of the global communication provided by virtual nodes, we develop a distributed equivariant GNN, called DistEGNN, which not only improves computational efficiency but also maintains strong predictive performance. Our method fuses both data parallelism and model parallelism. On one hand, a large graph is partitioned into multiple subgraphs, each processed independently by a model replica on a separate device. On the other hand, we use virtual nodes as communication intermediaries across devices, and the model's computation inherently depends on the flow of information between the devices.

Specifically, as illustrated in Fig. 2, for an extremely large graph that cannot fit into the memory of a single device, we firstly use a graph partition method to map each node to distinct computing device. We explore two types of graph partition methods: the trivial random partition and the METIS [31] algorithm. Subsequently, each device constructs its own local graph based on the nodes distributed to it. Besides the real nodes, we also initialize a shared, ordered set of virtual nodes on each local graph to enable cross device message passing. It is worth noting that, we still initialize the positions of the virtual nodes at the CoM of the entire large graph in DistEGNN. This initialization preserves translation equivariance of our model.

During the training process, each device independently conducts parallel message passing on its assigned local graph. Meanwhile, the virtual nodes are kept synchronizing across devices in real time, ensuring seamless propagation of global information across partitions. Formally, the computations of real-real message, virtual global message, and real-virtual message follow Eqs. (3) to (5), while the real aggregation process adheres to Eqs. (6) and (7). These operations are identical to those in the single-device version and can be executed in parallel on each device for the corresponding local subgraphs. By contrast, updating the virtual nodes in the distributed version requires aggregating messages from all real nodes across all devices. To formalize this, let D denote the total number of the used devices, and n_d indicates the index of each real node in the d -th device. The update for the virtual nodes in the distributed scenario is given by:

$$\bar{\mathbf{z}}_c^{(l+1)} = \bar{\mathbf{z}}_c^{(l)} + \frac{1}{N} \sum_{d=1}^D \sum_{n_d=1}^{N_d} (\bar{\mathbf{z}}_c^{(l)} - \bar{\mathbf{x}}_{n_d}^{(l)}) \varphi_Z(\mathbf{m}_{n_d c}^v), \quad (16)$$

$$\mathbf{s}_c^{(l+1)} = \mathbf{s}_c^{(l)} + \varphi_S \left(\mathbf{s}_c^{(l)}, \frac{1}{N} \sum_{d=1}^D \sum_{n_d=1}^{N_d} \mathbf{m}_{n_d c}^v \right), \quad (17)$$

where $\sum_{d=1}^D$ denotes summation across devices, and this requires communication between devices.

The learning objective in Eq. (11) is distributable across multiple devices. To be specific, we compute the loss of the d -th device in parallel as follows:

$$\mathcal{L}_d = \mathcal{L}_{\text{MSE}}(\bar{\mathbf{X}}_d^{(L)}, \bar{\mathbf{X}}_d^{\text{GT}}) + \lambda \mathcal{L}_{\text{MMD}}(\bar{\mathbf{Z}}^{(L)}, \bar{\mathbf{X}}_d^{\text{GT}}), \quad (18)$$

where $\bar{\mathbf{X}}_d^{(L)}$ and $\bar{\mathbf{X}}_d^{\text{GT}}$ respectively denote the predicted and the ground-truth node coordinates in the d -th device.

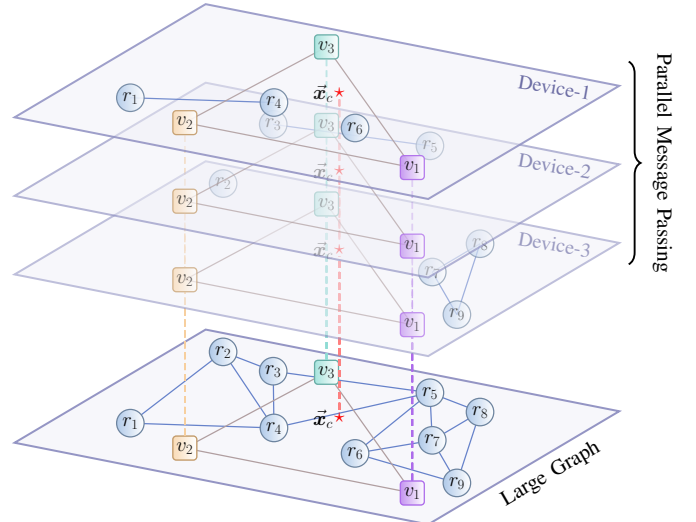


Fig. 2. Overview of DistEGNN. Multiple devices collaboratively process a large graph in parallel. The core of our design is the shared virtual nodes across devices, which propagate global information and mitigate the performance loss caused by graph partitioning.

PyTorch provides a function defined as `all_reduce` to aggregate information across devices. However, it is important to note that, in its implementation, gradients do not propagate

back through the collective communication path to each individual device. This behavior leads to disrupted gradient flow in scenarios where the result of the reduction operation participates in subsequent gradient computations in Eqs. (16) and (17). To address this issue, we implement a custom cross-device aggregation operation with explicitly defined forward and backward behaviors. In the forward pass, the operation performs distributed summation across devices, while in the backward pass, it ensures gradients are correctly redistributed and propagated back to all contributing devices. This design helps to preserve full computational graph in the distributed environment. During training, each device computes the loss independently based on its local subgraph, while our customized method guarantees correct gradient backpropagation across distributed devices. For inference, since gradient computation is unnecessary, we disable gradient tracking for improved efficiency.

The pseudocode for training DistEGNN is provided in Algorithm 1.

Algorithm 1: Training DistEGNN on D Devices.

Data: Large graph $\vec{\mathcal{G}} = (\vec{\mathbf{X}}, \mathbf{H}; \mathcal{E})$.
Result: Trained DistEGNN model with L layers.
 // Initialization.

- 1 Initialize virtual nodes coordinates $\vec{\mathbf{Z}} = \frac{1}{N} \sum_{i=1}^N \vec{\mathbf{x}}_i \mathbf{1}^\top$, learnable features $\mathbf{S} \in \mathbb{R}^{H \times C}$;
- 2 Partition $\vec{\mathcal{G}}$ into D parts and construct subgraphs with the shared virtual nodes, assigning $\vec{\mathcal{G}}_1^v, \dots, \vec{\mathcal{G}}_D^v$ to D devices;
 // Parallel Message Passing.
- 3 **for** $l = 1$ to L **do**
- 4 Center of graph $\vec{\mathbf{x}} = \frac{1}{N} \sum_{d=1}^D \left(\sum_{n_d=1}^{N_d} \vec{\mathbf{x}}_{n_d} \right)$;
- 5 Calculate message using Eqs. (3) to (5);
 // For Real Nodes.
- 6 Aggregate and update with Eqs. (6) and (7);
 // For Virtual Nodes.
- 7 Aggregate and update with Eqs. (16) and (17);
- 8 **end**
 // Calculate loss and update model.
- 9 Calculate local loss \mathcal{L}_d with Eq. (18) and compute gradients $\nabla_{\theta} \mathcal{L}_d$ on each device;
- 10 Synchronize gradients across devices to get $\nabla_{\theta} \mathcal{L}$;
- 11 Update model parameters on each device:
 $\theta \leftarrow \theta - \eta \nabla_{\theta} \mathcal{L}$;

VII. EXPERIMENTS

In this section, we conduct comprehensive experiments to evaluate the **effectiveness** of FastEGNN, the **generalizability** of our virtual node module and the **scalability** of DistEGNN on challenging physical simulation tasks over large geometric graphs. We begin by introducing the datasets used in our experiments in Section VII-A. Then, in Section VII-B, we demonstrate the effectiveness of our proposed FastEGNN through benchmark comparisons and ablation studies. In Section VII-C, we examine the generalizability of the proposed

virtual node mechanism by applying it to other representative models, leading to FastRF, FastSchNet, and FastTFN. Finally, we evaluate the efficiency and efficacy of the DistEGNN on our generated extremely large graph dataset in Section VII-D.

A. Dataset Details

We comprehensively benchmark FastEGNN on three challenging simulation datasets to evaluate its effectiveness and generalizability. Additionally, we introduce a fourth dataset of custom-generated large-scale graphs (with 113K nodes per graph on average), designed to assess the scalability of DistEGNN.

N -body System [9, 32]. In this simulation, each system comprises $N = 100$ charged particles with random charge $c_i \in \{\pm 1\}$, whose movements are driven by coulomb force. The graph is constructed in a fully-connected manner. We use 5,000 samples for training, 2,000 for validation, and 2,000 for testing. The task is to predict the particle positions at frame 40 given their positions and velocities at frame 30.

Protein Dynamics [33]. The protein molecular dynamics dataset is processed from MDAnalysis [34], which depicts a long-range AdK equilibrium MD trajectory [35]. Following previous work [33], we model the dynamics of the backbone atoms, leading to 855 nodes per sample. A total number of 55,108 edges (on average) are connected between the atoms within a distance cutoff of 10Å. The dataset has been split into train/validation/test sets that contain 2,481/827/878 frame pairs, respectively, with the time span $\Delta t = 15$.

Water-3D [36]. Water-3D is a large-scale particle-based fluid simulation dataset generated with Smoothed-Particle Hydrodynamics (SPH). The dataset records the dynamics of water falling in a box, with 1000 trajectories for training, 100 for validation, and 100 for testing. There are on average a large amount of 7,806 particles and 94,931 edges in each system, where the edges are connected with a cutoff of 0.035. The prediction task involves forecasting particle positions with a time span of $\Delta t = 15$ frames. It serves as a challenging benchmark for FastEGNN.

Fluid113K [37]. Fluid113K is an extremely large-scale particle-based fluid simulation dataset constructed based on the open source implementation from DeepLagrangianFluids [37]. The simulation is performed within the SPLisHSPlasH [38] framework, which enables high-fidelity modeling of incompressible fluid dynamics. We adopt the scenario in which a single fluid body falls inside a standard cubic container. To increase the scale of each simulation, we enlarge both the particle size and container size, ensuring that each trajectory contains more than 100,000 particles. In total, we generate 100 trajectories for training, 20 for validation, and 20 for testing. Each trajectory simulates 4 seconds of motion, recorded at 50 Hz, resulting in 200 frames. During training, we randomly sample 16 starting time steps from each trajectory and set the prediction interval to $\Delta t = 20$. On average, each frame contains 113,140 particles and 1,706,973 edges. As an exceptionally large graph dataset, Fluid113K poses significant challenges for evaluating the scalability of geometric graph neural networks. The data generation process may take approximately a week to complete, depending on the CPU performance.

TABLE I

RESULTS OF FASTEGNN AND BASELINES ON N -BODY SYSTEM (100 NODES), PROTEIN DYNAMICS (855 NODES), AND WATER-3D (7806 NODES) DATASETS. FASTEGNN- $\langle C, p \rangle$ DENOTES THE MODEL WITH THE NUMBER OF VIRTUAL NODES AS C AND EDGE DROPPING RATE AS p . WE ALSO REPORT THE RESULTS OF EGNN* WHICH INDICATES THE EGNN MODEL WITH ALL EDGES DROPPED.

	N -body System		Protein Dynamics		Water-3D	
	MSE ($\times 10^{-2}$)	Relative Time	MSE	Relative Time	MSE ($\times 10^{-4}$)	Relative Time
Linear	12.66	0.01	2.26	0.01	14.06	0.01
MPNN [21]	3.06	0.62	150.56	0.62	5299.30	0.61
SchNet [13]	24.83	1.39	2.56	1.40	35.02	2.44
RF [18]	5.76	0.26	2.25	0.25	12.94	0.25
TFN [15]	1.62	17.02	2.26	17.81	9.10	19.53
EGNN [9]	1.41	1.00	2.25	1.00	6.00	1.00
EGNN* [9]	11.62	0.03	2.26	0.06	12.38	0.11
FastEGNN- $\langle 1, 0.00 \rangle$	1.04	1.15	1.89	1.15	3.25	1.35
FastEGNN- $\langle 1, 0.75 \rangle$	1.03	0.32	1.91	0.65	3.64	0.47
FastEGNN- $\langle 1, 1.00 \rangle$	9.72	0.07	2.00	0.12	4.36	0.22
FastEGNN- $\langle 3, 0.00 \rangle$	1.06	1.19	1.82	1.23	2.58	1.51
FastEGNN- $\langle 3, 0.75 \rangle$	1.09	0.36	1.85	0.72	3.13	0.65
FastEGNN- $\langle 3, 1.00 \rangle$	9.52	0.11	1.92	0.18	3.60	0.40
FastEGNN- $\langle 10, 0.00 \rangle$	1.10	1.36	1.84	1.47	2.66	1.81
FastEGNN- $\langle 10, 0.75 \rangle$	0.99	0.53	1.88	0.98	2.94	0.85
FastEGNN- $\langle 10, 1.00 \rangle$	9.25	0.27	1.99	0.43	3.40	0.61

B. Effectiveness of FastEGNN

Implementation Details To evaluate the effectiveness of our method, we instantiate several variants of FastEGNN by exploring different combinations of the number of virtual nodes C and the edge dropping rate p , denoted as FastEGNN- $\langle C, p \rangle$. We adopt the following edge dropping strategy: We sort all edges based on the distance between the connected nodes $\|\vec{x}_i - \vec{x}_j\|_2$ and drop the top p ($\times 100\%$) longest edges.

Baselines. We compare our models with the following baselines: the simplest equivariant model Linear dynamics [9], the non-equivariant Message-Passing Neural Network (MPNN) [21], the invariant GNN model SchNet [13], and the equivariant GNNs including Tensor Field Networks (TFN) [15], Radial Field (RF) [18], and EGNN [9]. We also evaluate EGNN*, a variant of EGNN that removes all edges in the graph, as a reference.

Metrics. 1. MSE: We use the Mean Squared Error (MSE) between the predicted position and the ground truth on the testing set as the metric to measure the prediction accuracy. Note that we add random rotations on input and target graph during testing to assess the model’s equivariance. **2. Relative Time:** To demonstrate the speed-up effect of FastEGNN, we also benchmark the inference time of all models to traverse through the entire testing set, and compute their relative scales *w.r.t.* the inference time of EGNN.

1) Main Results

The main quantitative results are presented in Table I. We have the following observations:

1. Our FastEGNN yields the lowest simulation error on all three benchmarks, consistently outperforming the competitive baselines by a significant margin. For instance, FastEGNN yields 29% and 19% improvement in terms of MSE over the best-performed baseline EGNN on N -body system and Protein Dynamic datasets, respectively. On the most challenging dataset Water-3D with an average of 7,806 particles in each system, FastEGNN reaches a remarkably low simulation error of $2.58 \times$

10^{-4} , as opposed to EGNN with an MSE of 6.00×10^{-4} . The strong results unanimously demonstrate the superiority of FastEGNN in learning to simulate physical dynamics and especially scaling to large and complicated systems.

2. With the help of edge dropping, FastEGNN is able to conduct inference in a substantially faster manner. Such effect is evident in the Relative Time metric, where FastEGNN with an edge dropping rate of 0.75 or 1.00 increase the inference speed. Notably, FastEGNN with 10 virtual nodes and 75% of the edges dropped delivers the lowest MSE on N -body system while only using 53% of the inference time of EGNN.

3. When all edges are preserved, FastEGNN performs favorably across all datasets compared with EGNN, thanks to the proposed virtual node learning technique that boosts the model expressivity. Interestingly, we also observe that the performance is only slightly affected even when a large proportion of the edges are dropped. Even in the extreme case where all edges are removed, FastEGNN still achieves competitive results. For example, on the Water-3D dataset, FastEGNN- $\langle 3, 1.00 \rangle$ with all edges dropped still obtains an MSE of 3.60, remarkably lower than the MSE of 6.00 produced by EGNN. By contrast, EGNN* performs poorly in all cases, with performance close to Linear Dynamics. Overall, the results show that our virtual learning enhances the expressivity of the model and improves the performance, while also enabling edge dropping for higher inference speed with minimal sacrifice in prediction accuracy.

2) Rollout Experiment

To further evaluate the robustness and accuracy of our model, we design a rollout experiment. In this setup, the model recursively uses its own predictions as inputs for the subsequent step. Compared to single-step prediction, this setting is more challenging, as prediction errors can accumulate and intensify throughout the rollout process.

We evaluate the rollout performance of EGNN and FastEGNN- $\langle 10, 0.75 \rangle$ by performing five consecutive rollout

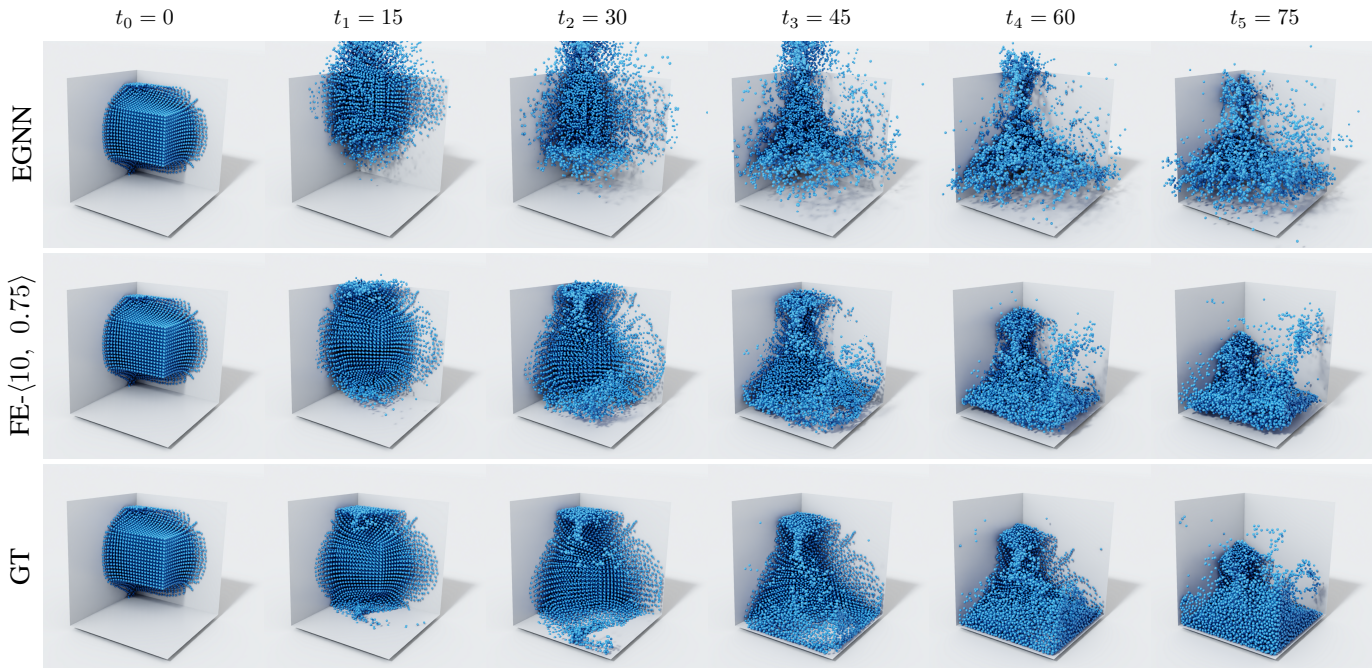


Fig. 3. Rollout results of EGNN and FastEGNN-(10, 0.75) (abbreviated as FE-(10, 0.75) for brevity) on Water-3D dataset. After the fluid hits the box, EGNN exhibits unstable predictions, whereas our model produces results that match the ground truth more closely.

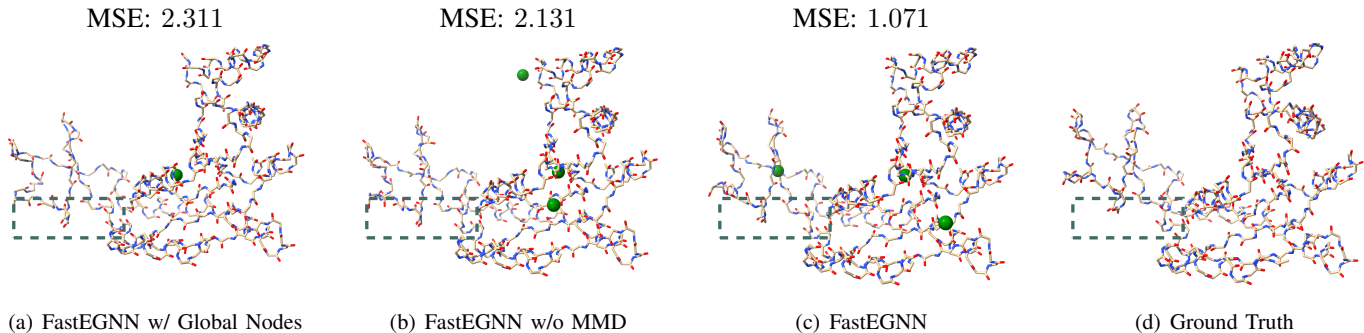


Fig. 4. The results of different variants of FastEGNN on Protein Dynamics. We use green dots to indicate the learned locations of the virtual nodes. The dashed box marks highlight the region of interest where FastEGNN yields more accurate prediction. For FastEGNN w/ Global Nodes, the learned coordinates of 3 virtual nodes are almost the same.

steps for each model. The time span between rollout steps is $\Delta t = 15$ frames (corresponding to 0.075 seconds), which is consistent with the configuration in our main experiments. We render the fluid shape at each step, as shown in Fig. 3. From the visualizations, we can observe that EGNN’s predictions are highly unstable: the predicted particles are spatially dispersed, with many of them escaping far beyond the boundaries of the container. In contrast, FastEGNN yields much more stable and accurate results, with the predicted fluid shapes closely matching the ground truth. This indicates that FastEGNN can better capture the inherent physical laws.

3) Ablation Studies

The number of virtual nodes. We investigate the effect of the number of virtual nodes together with the edge dropping rate on three datasets. We sweep the number of virtual nodes in $\{1, 3, 10\}$ and the edge dropping rate in $\{0.00, 0.75, 1.00\}$, with the detailed results shown in Table I. We also involve the results of EGNN with the same edge dropping rates for reference. It is clear that, under the same edge dropping rate, FastEGNN

consistently outperforms EGNN in terms of prediction accuracy, benefiting from the incorporation of virtual nodes. In addition, it introduces only a marginal increase in inference time, owing to our efficient design of message computation and aggregation scheme for virtual nodes.

Notably, we observe that increasing the number of virtual nodes does not always lead to better performance. On the Protein Dynamics and Water-3D datasets, the best accuracy is achieved when using three virtual nodes, while the performance slightly degrades when the number increases to ten. This suggests that a limited number of virtual nodes is sufficient to enhance model performance, whereas an excessive number may introduce redundancy and reduce effectiveness.

Modeling virtual nodes as ordered set. We have proposed to model the virtual nodes as an ordered set instead of an unordered set, which enforces mutual distinctiveness as an inductive bias. We demonstrate the validity of such a design in Table II, where we implement a variant of FastEGNN

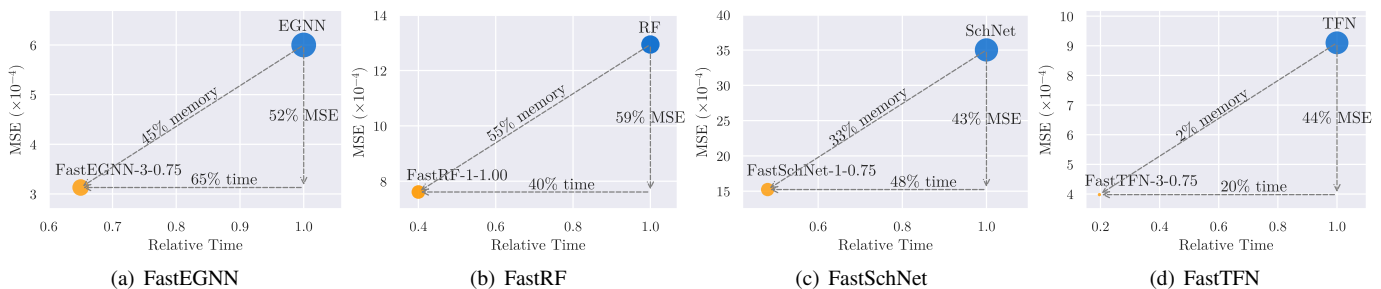


Fig. 5. The performance of four base and enhanced models on the Water-3D dataset in terms of speed, accuracy, and memory. Points closer to the lower-left corner and smaller in size indicate better overall efficiency.

TABLE II

ABLATION STUDIES ON THE DESIGN OF VIRTUAL NODE LEARNING. EXPERIMENTS ARE CONDUCTED ON PROTEIN DYNAMICS DATASET AND ALL VARIANTS OF FASTEGNN IN THIS EXPERIMENT CONTAINS 3 VIRTUAL NODES.

Model Setting	Dropping Rate		
	0.00	0.75	1.00
EGNN	2.250	2.244	2.257
FastEGNN w/ Global Nodes	1.950	1.967	2.121
FastEGNN w/o MMD	1.857	1.926	1.975
FastEGNN	1.821	1.852	1.919

referred to as *FastEGNN w/ Global Nodes*, which treats virtual nodes as global nodes with permutation-equivariant message passing in between.

We discover that naively viewing them as global nodes leads to worse performance and indistinguishable assignment of the virtual nodes (Fig. 4(a)). Their MSE is consistently higher than that of the original FastEGNN. Moreover, the performance drops sharply as the dropping rate increases from 0.00 to 1.00, with MSE rising from 1.950 to 2.121. In contrast, our approach endows virtual nodes with orders and different roles, resulting in generally lower MSE.

The impact of MMD loss. As described in Section IV-C, we introduce the MMD loss to enhance the mutual distinctiveness and global distributedness of virtual nodes, encouraging them to perform diverse and complementary roles. To assess its impact, we implement a variant without the MMD regularization, referred to as *FastEGNN w/o MMD*. As shown in Table II, removing the MMD loss during training results in a clear drop in performance. On the Protein Dynamic dataset, the model exhibits an average performance decline of an average drop of 3% across all three edge dropping rates. This limitation is also visually evident in Fig. 4. As shown in panel (b), without the MMD loss, all three virtual nodes are located on the right-hand side of the protein structure, failing to capture its overall geometry. In contrast, with MMD applied, FastEGNN (Fig. 4(c)) learns a more geometrically meaningful distribution of virtual nodes that better reflects the spatial characteristics of the underlying data.

C. Generalizability of FastEGNN

To validate the generalizability of our proposed virtual node mechanism, we extend it to three representative geometric GNNs with distinct architectures: RF [18], SchNet [13], and TFN [15], leading to the enhanced variants FastRF, FastSchNet, and FastTFN. The coordinate update equations for these enhanced models are detailed in Section V.

We evaluate the performance of baseline and enhanced models on N -body, Protein Dynamics, and Water-3D dataset under the same setups and metrics as described in Section VII-B. Each enhanced model includes 9 variants, constructed by combining three different numbers of virtual nodes $\{1, 3, 10\}$ with three edge dropping rates $\{0.00, 0.75, 1.00\}$. The results are detailed in Table III.

We further visualize the improvements in speed, accuracy, and memory usage of the four enhanced models compared to their corresponding base models, as shown in Fig. 5. We can observe that, by introducing virtual nodes and applying edge dropping, all four enhanced models achieve significant improvements in both accuracy and efficiency. For example, the FastRF-1-1.00 achieves 59% of RF’s MSE while using only 40% of the training time and 55% of the memory. Moreover, compared to the resource-intensive TFN, FastTFN uses only 2% of the memory and 20% of the computation time, while reducing prediction error by 56%. These examples consistently demonstrate the advantages of our approach.

Of all 36 experimental configurations, the only unexpected case where the baseline model outperforms its enhanced version is TFN on the N -body dataset without edge dropping. One possible reason is that, during the construction of FastTFN, we reduced the number of channels in the TFN layer from 32 to 1 for lower computational cost and better compatibility, which in turn weakened its ability to simulate the N -body dataset. However, we find that TFN is highly sensitive to graph connectivity. When the edge dropping rate increases to 0.75, the MSE sharply rises from 1.62 to 4.53. In contrast, FastTFN exhibits greater robustness in such settings. With 75% of the edges dropped, FastTFN reverses the performance gap and achieves better accuracy than TFN. This demonstrates that the virtual node mechanism effectively mitigates the impact of missing connections and enhances the model’s expressiveness and stability on sparse graphs.

TABLE III

COMPARISONS BETWEEN EGNN [9], RF [18], SchNet [13], TFN [15] AND THEIR ENHANCED MODELS INVOLVING VIRTUAL NODE LEARNING. NOTE THAT THE TFN SERIES DOES NOT SUPPORT THE EDGE DROPPING RATE OF 1.00, AS THE INITIALIZATION VIA SPHERICAL HARMONICS REQUIRES THE PRESENCE OF EDGES.

Dropping Rate	N -body System ($\times 10^{-2}$)			Protein Dynamics			Water-3D ($\times 10^{-4}$)		
	0.00	0.75	1.00	0.00	0.75	1.00	0.00	0.75	1.00
EGNN [9]	1.30	1.34	11.62	2.25	2.24	2.26	6.00	9.87	12.38
FastEGNN-1	1.04	1.03	9.72	1.89	1.91	2.00	3.25	3.64	4.36
FastEGNN-3	1.06	1.09	9.52	1.82	1.85	1.91	2.58	3.13	3.60
FastEGNN-10	1.10	0.99	9.25	1.84	1.88	1.99	2.66	2.94	3.40
RF [18]	5.76	5.77	11.65	2.25	2.26	2.26	12.94	12.10	12.49
FastRF-1	4.17	4.19	10.22	2.18	2.21	2.21	7.33	7.31	7.61
FastRF-3	4.13	4.90	10.24	2.19	2.21	2.21	7.71	7.35	7.97
FastRF-10	4.04	4.24	10.20	2.19	2.21	2.21	7.72	7.90	8.04
SchNet [13]	24.83	25.80	35.49	2.56	2.56	2.60	35.02	52.73	57.81
FastSchNet-1	23.61	23.70	25.96	2.01	2.03	2.22	14.29	15.23	18.69
FastSchNet-3	23.60	23.59	25.95	1.98	2.08	2.14	13.36	13.16	15.14
FastSchNet-10	23.73	23.80	25.97	1.99	2.05	2.11	14.38	13.09	13.94
TFN [15]	1.62	4.53	–	2.25	2.26	–	9.10	15.91	–
FastTFN-1	3.42	4.34	–	1.90	1.99	–	3.89	5.15	–
FastTFN-3	3.42	3.65	–	1.86	1.92	–	3.33	3.98	–
FastTFN-10	3.87	3.99	–	1.92	1.95	–	3.15	3.61	–

D. Evaluation of DistEGNN

In Section VI, we present a distributed approach for geometric GNNs based on graph partitioning. This method significantly enhances the model’s scalability, making it feasible to simulate geometric graphs with millions of edges. In this section, we design a set of challenging experiments to validate the advantages of DistEGNN in terms of computational overhead and prediction accuracy. The experiment setup and corresponding results are detailed below.

1) Implementation Details

We evaluate the performance of EGNN and DistEGNN on two datasets: Water-3D and Fluid113K. Fluid113K is our generated extremely large scale dataset, with each graph contains over 100K nodes and more than 1M edges. Simulating such large-scale graphs requires over 40GB of memory even with a batch size of 1, making it impossible to run on single low-memory device such as a NVIDIA-V100-32G. However, with our distributed strategy, the memory burden on each device is greatly reduced, enabling multiple low-memory devices to jointly simulate one large graph.

For the Water-3D dataset, we set the batch size to 16 and the virtual nodes to $\{1, 3, 10\}$. For Fluid113K, we use a batch size of 1 and fix the number of virtual nodes to 5. Each model is trained using 1 to 8 computing devices. To measure relative inference time and peak memory usage per device, we perform training and inference for 14 times in a consistent environment, discard the two highest and two lowest values, and report the average of the remaining runs as the final result.

We use random graph partitioning as the default strategy, where each node has an equal probability of being assigned to any computing device. The impact of alternative partitioning methods on model performance is analyzed in Section VII-D4. After partitioning, each device contains nodes with lower spatial density. We still apply the same cutoff radius for edge construction as in the single-device setting by default. This improves the speedup ratio but poses a significant challenge to the model’s performance on these sparse graphs. Moreover,

we also explore dynamically adjusting the cutoff radius based on the sparsity of the graph in ablation study, with results presented in Table VII.

2) Main Results

Our detailed experimental results are presented in Tables IV and V. For better illustration, we visualize the inference time, accuracy, and the peak memory usage across different models in Fig. 6. The analysis of the results leads to the following conclusions:

1. Our enhanced model consistently demonstrates better prediction accuracy than EGNN. As the Fig. 6 shows, the worst result of the DistEGNN still surpasses the best performance achieved by EGNN. For instance, DistEGNN-3 achieves a MSE of 3.27 on the Water-3D dataset even when running in parallel on 8 computing devices, which is substantially lower than EGNN’s best result of 6.00 under a single-device setup. In addition, its inference time is reduced to just 49% of that required by the single-device EGNN.

2. Our distributed parallelization approach significantly reduces both computational time and memory consumption, making it feasible to simulate extremely large graphs using multiple less powerful devices with limited memory. As shown in Table V, processing a single graph of Fluid113K by one device requires 42GB and 48GB of memory for EGNN and DistEGNN-5, respectively. These memory requirements exceed the capabilities of many common devices. With our distributed strategy applied, both time and memory costs are significantly reduced in practice. For example, the training time of DistEGNN-5 with two cooperating devices is reduced to 48%, resulting in a $2.06\times$ speedup. The memory usage per device also drops from about 48GB to 16GB, representing a 67% reduction. When using 8 devices, the training becomes $7.34\times$ faster, and the memory required per device is reduced to only 1.58GB, making it possible to simulate graphs with over 100,000 nodes using minimal resources.

3. Our virtual nodes effectively mitigate performance degradation caused by graph partitioning. As shown in Fig. 6, when the number of computing devices increases from 1 to

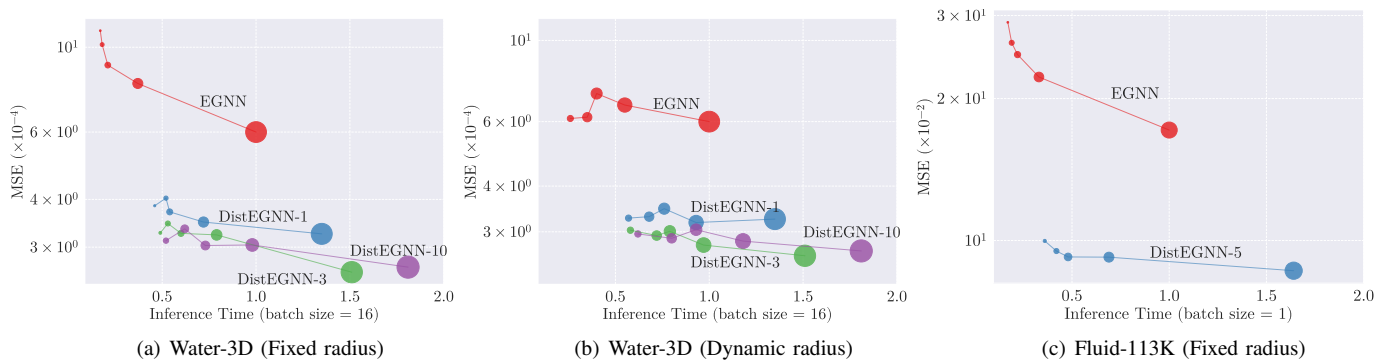


Fig. 6. Visualization of inference time, accuracy, and memory usage of EGNN [9] and DistEGNN. The larger circles indicate higher memory usage. For each model, we visualize the results on 1, 2, 3, 4, and 8 devices.

8, EGNN exhibits a much more severe performance drop compared to DistEGNN. Quantitatively, on the Water-3D dataset, EGNN’s performance declines by 84% under the 8 devices setting, while DistEGNN-10 incurs only a 17% loss. On the Fluid113K dataset, DistEGNN demonstrates even stronger robustness: EGNN experiences a 69% drop in accuracy, whereas DistEGNN-5 exhibits a minor reduction of just 15%. We attribute this advantage to the global information transmitted by virtual nodes across devices, which effectively bridges the information gap between subgraphs caused by distributed graph partitioning. This allows DistEGNN to maintain high accuracy under distributed settings, enhancing both scalability and practical applicability.

4. Moderately increasing the number of virtual nodes leads to noticeable improvements in model performance. As shown in Fig. 6(a), the curve for DistEGNN-3 lies below that of DistEGNN-1. This indicates that increasing the number of virtual nodes generally enhances the model’s prediction accuracy. However, further increasing the number of virtual nodes from 3 to 10 brings in minor benefits. At the same time, thanks to our efficient implementation of message construction and aggregation, this increase in virtual nodes introduces only limited computational overhead. This makes it worthwhile to use more virtual nodes in exchange for improved accuracy. For instance, in the 8 device setting, DistEGNN-10 incurs just 13% more inference time than DistEGNN-1, yet achieves a 23% gain in prediction accuracy.

3) Rollout Experiment

We further evaluate the performance of DistEGNN and EGNN on rollout experiments under the distributed setting. We conduct this experiment on the test set of Fluid113K dataset with 8 devices collaboratively simulate a large graph. Results are visualized in Fig. 7.

As shown in the figure, the predictions of DistEGNN-5 align more closely with the ground truth compared to those of EGNN. This is particularly evident in the upper region of the box, where DistEGNN shows significantly higher accuracy in capturing the shape of the splashing water, resulting in a more faithful representation of the fluid’s state after impacting the container. In contrast, EGNN’s results tend to accumulate at the bottom of the box, with many particles dispersing beyond the container boundaries, failing to accurately reflect the underlying physical process.

4) Ablation Studies

Graph partition strategy. The choice of graph partitioning strategy could affect model performance in distributed settings. By default, we adopt a random partitioning strategy, where each node is randomly assigned to one of the computing devices with equal probability. This method is simple to implement, computationally efficient, and allows flexible adjustment of assignment probabilities when there is performance variation among devices.

We also investigate the impact of alternative partitioning strategies on the Water-3D dataset, but observe no significant performance differences. For instance, METIS [31] is a widely used graph partitioning algorithm. It seeks to preserve as many internal edges as possible while ensuring that each partition contains a balanced number of nodes. We initially expected that such a method would reduce the information loss caused by partitioning. However, our experiments show that applying METIS to the Water-3D dataset does not yield noticeable performance gains, as reported in Table VI.

This may be attributed to the absence of clear community structures or localized density in the dataset, resulting in a similar edge retention rate between the METIS and random partitioning strategies. In addition, compared to the random strategy, METIS introduces additional computational overhead, which increases the setup time before distributed training. Therefore, considering partitioning quality and system efficiency, we continue to use the random partitioning strategy as the default in our experiments. In the context of large-scale graph data with clear structural patterns, we believe that further exploration of structure-aware partitioning methods remains essential for improving the efficiency and performance of distributed training.

Cutoff radius. By default, we use a fixed cutoff radius to construct graphs on each device. Although this significantly reduces the number of edges and benefits model execution speed, it also poses a considerable challenge to the model’s expressiveness. To avoid this potential performance loss, we explore increasing the cutoff radius in distributed graphs to keep more connections.

We conduct a new set of experiments, in which the cutoff radius is dynamically adjusted during multi-device parallel execution. Specifically, when running on multiple devices, we increase the cutoff radius in steps of 0.001 until the total edge

TABLE IV
PERFORMANCE OF EGNN [9] AND DISTEGNN ON THE WATER-3D DATASET USING THE FIXED CUTOFF RADIUS FOR GRAPH CONSTRUCTION.

		1-device	2-devices	3-devices	4-devices	5-devices	6-devices	7-devices	8-devices
Graph information	Cutoff radius	0.035	0.035	0.035	0.035	0.035	0.035	0.035	0.035
	Edge count	94931	23711	10548	5930	3794	2637	1936	1481
	Average degree	12.16	3.04	1.35	0.76	0.49	0.34	0.25	0.19
MSE ($\times 10^{-4}$)	EGNN [9]	6.00	8.04	8.98	10.16	10.95	10.57	11.03	11.05
	DistEGNN-1	3.25	3.49	3.71	4.03	4.00	3.87	4.11	3.85
	DistEGNN-3	2.58	3.23	3.26	3.46	3.47	3.19	3.45	3.27
	DistEGNN-10	2.66	3.04	3.03	3.35	3.34	3.15	3.46	3.12
Relative training time	EGNN [9]	1.00	0.37	0.21	0.18	0.16	0.16	0.16	0.17
	DistEGNN-1	1.69	0.91	0.66	0.60	0.53	0.52	0.52	0.54
	DistEGNN-3	1.97	1.06	0.76	0.64	0.58	0.56	0.55	0.57
	DistEGNN-10	2.77	1.51	1.05	0.86	0.75	0.70	0.68	0.66
Relative inference time	EGNN [9]	1.00	0.37	0.21	0.18	0.17	0.16	0.17	0.17
	DistEGNN-1	1.35	0.72	0.54	0.52	0.48	0.47	0.47	0.46
	DistEGNN-3	1.51	0.79	0.60	0.53	0.49	0.48	0.49	0.49
	DistEGNN-10	1.81	0.98	0.73	0.62	0.56	0.54	0.53	0.52
Device memory usage (GB)	EGNN [9]	74.15	17.23	5.63	2.60	1.90	1.14	0.68	0.50
	DistEGNN-1	75.66	17.93	6.11	3.05	2.12	1.34	1.00	0.76
	DistEGNN-3	78.09	19.32	6.42	4.31	3.36	2.45	1.70	1.40
	DistEGNN-10	84.26	27.63	13.30	10.66	10.63	7.15	7.31	4.89
Total memory usage (GB)	EGNN [9]	74.15	34.45	16.88	10.40	9.52	6.86	4.76	3.98
	DistEGNN-1	75.66	35.86	18.33	12.22	10.59	8.07	7.00	6.08
	DistEGNN-3	78.09	38.65	19.25	17.22	16.80	14.70	11.89	11.21
	DistEGNN-10	84.26	55.26	39.90	42.64	53.16	42.91	51.16	39.10

TABLE V
PERFORMANCE OF EGNN [9] AND DISTEGNN ON FLUID113K DATASET USING THE FIXED CUTOFF RADIUS FOR GRAPH CONSTRUCTION.

		1-device	2-devices	3-devices	4-devices	5-devices	6-devices	7-devices	8-devices
Graph information	Cutoff radius	0.075	0.075	0.075	0.075	0.075	0.075	0.075	0.075
	Edge count	1706973	426430	189639	106615	68233	47387	34851	26676
	Average degree	15.09	3.76	1.68	0.94	0.60	0.41	0.31	0.24
MSE ($\times 10^{-2}$)	EGNN [9]	17.15	22.22	24.79	26.26	27.50	28.34	29.43	29.02
	DistEGNN-5	8.63	9.22	9.23	9.50	10.46	10.06	10.08	9.98
Relative training time	EGNN [9]	1.00	0.35	0.21	0.17	0.14	0.14	0.15	0.15
	DistEGNN-5	6.10	2.96	1.95	1.44	1.15	1.00	0.90	0.83
Relative inference time	EGNN [9]	1.00	0.33	0.22	0.19	0.15	0.15	0.16	0.17
	DistEGNN-5	1.64	0.69	0.48	0.42	0.36	0.35	0.35	0.36
Device memory usage (GB)	EGNN [9]	41.55	15.00	6.20	4.00	2.02	1.22	0.69	0.47
	DistEGNN-5	47.97	15.89	9.37	4.19	3.09	3.02	2.11	1.58
Total memory usage (GB)	EGNN [9]	41.55	30.01	18.57	15.98	10.09	7.32	4.82	3.77
	DistEGNN-5	47.97	31.77	28.11	16.77	15.47	18.12	14.80	12.62

TABLE VI
MSES OF EGNN AND DISTEGNN UNDER RANDOM AND METIS PARTITIONING METHODS.

	2-devices	3-devices	4-devices
Graph Attributes			
Edges (random)	23711	10548	5930
Edges (METIS)	24336	11004	6282
MSE Results			
EGNN (random)	8.04	8.98	10.16
EGNN (METIS [31])	7.77	9.06	10.57
DistEGNN-3 (random)	3.23	3.26	3.46
DistEGNN-3 (METIS [31])	3.37	3.05	3.04

count in the distributed graph approximates that of the single-device graph. Under the new radius, we retrain DistEGNN on the Water-3D dataset using 2 to 8 devices, with results reported

in Table VII. As the table shows, dynamically increasing the cutoff radius effectively alleviates the performance drop under multi-device parallel training. Notably, DistEGNN-1 experienced a maximum performance drop of only 6.77%, with the MSE increasing slightly from 3.25 to 3.47. When running on 8 devices, the MSE increases by merely 0.02, yet yielding a 2.77 times improvement in training speed. For a direct comparison, we visualize the results of the dynamic radius setting on the Water-3D dataset in Fig. 6(b), using the same coordinate scale as in Fig. 6(a). Comparing the two results, we observe that using a fixed radius in the distributed setting achieves higher speedup, while the dynamic radius setting delivers better predictive accuracy. These findings suggest that dynamically finetuning the cutoff radius for graph construction enables DistEGNN to effectively balance computational efficiency and prediction performance.

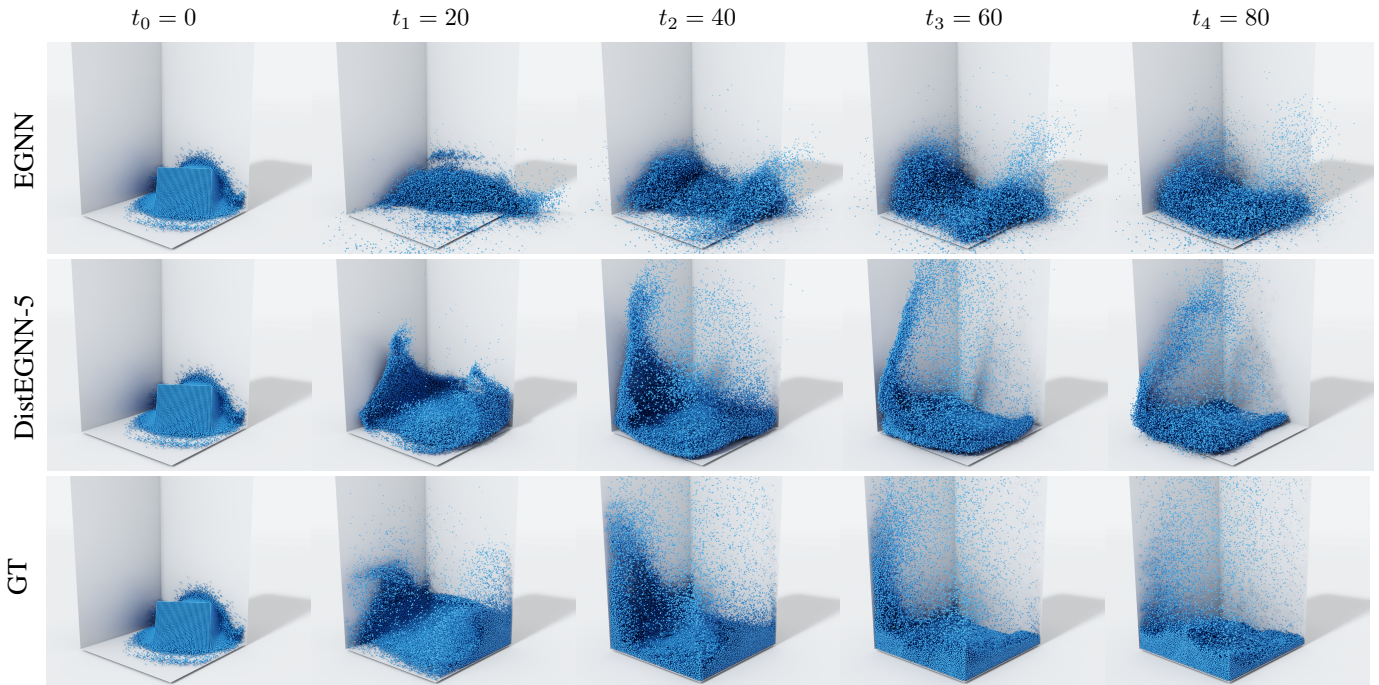


Fig. 7. Rollout results of EGNN and DistEGNN-5 on Fluid113K dataset, with training and inference performed in the distributed environment with 8 devices.

TABLE VII
PERFORMANCE OF EGNN [9] AND DISTEGNN ON WATER-3D DATASET WITH DYNAMIC CUTOFF RADUIS FOR GRAPH CONSTRUCTION.

		1-device	2-devices	3-devices	4-devices	5-devices	6-devices	7-devices	8-devices
Graph information	Cutoff radius	0.035	0.045	0.052	0.057	0.062	0.066	0.070	0.074
	Edge count	94931	95535	94155	93576	95576	93137	93276	95576
	Average degree	12.16	12.24	12.06	11.99	12.24	11.93	11.95	12.24
MSE ($\times 10^{-4}$)	DistEGNN-1	3.25	3.18	3.47	3.30	3.43	3.32	3.33	3.27
	DistEGNN-3	2.58	2.76	3.01	2.93	3.15	3.10	2.96	3.03
	DistEGNN-10	2.66	2.83	3.04	2.88	3.16	2.89	2.94	2.96
Relative training time	DistEGNN-1	1.69	1.18	0.92	0.79	0.70	0.65	0.62	0.61
	DistEGNN-3	1.97	1.31	1.00	0.85	0.74	0.70	0.66	0.64
	DistEGNN-10	2.77	1.76	1.31	1.09	0.93	0.84	0.80	0.75
Relative inference time	DistEGNN-1	1.35	0.93	0.76	0.68	0.62	0.58	0.56	0.57
	DistEGNN-3	1.51	0.97	0.79	0.72	0.64	0.60	0.57	0.58
	DistEGNN-10	1.81	1.18	0.93	0.80	0.71	0.66	0.64	0.62
Device memory usage (GB)	DistEGNN-1	75.66	35.61	21.42	15.02	13.78	7.57	8.53	6.54
	DistEGNN-3	78.09	36.71	22.21	15.60	14.29	8.02	8.85	6.84
	DistEGNN-10	84.26	38.33	22.76	15.48	15.13	8.98	10.62	6.93
Total memory usage (GB)	DistEGNN-1	75.66	71.22	64.25	60.08	69.11	45.47	59.68	52.35
	DistEGNN-3	78.09	73.42	66.64	62.41	71.44	48.10	61.95	54.71
	DistEGNN-10	84.26	76.66	68.30	61.90	75.68	53.85	74.36	55.41

VIII. CONCLUSION

We propose FastEGNN and DistEGNN, two advanced models that leverage virtual nodes to operate efficiently and effectively on large sparse geometric graphs. The core insight of FastEGNN lies in constructing an ordered set of virtual nodes that enjoys both mutual distinctiveness and global distributedness to perform expressive message passing. DistEGNN, the distributed version of FastEGNN, enables multiple devices collaboratively process an extremely large graph, while simultaneously leverage a shared set of virtual nodes to transfer global messages across devices. This further extends the model’s capability and scalability. Comprehensive evaluations on both small graph with 100 nodes and large scale graph with more than 100K nodes consistently demonstrate the

superiority of FastEGNN and DistEGNN in terms of achieving remarkably lower simulation error and offering substantial efficiency improvements due to sparsification and distribution.

ACKNOWLEDGEMENTS

This work was jointly supported by the following projects: the National Natural Science Foundation of China (No. 62376276); Beijing Nova Program (No. 20230484278); the Fundamental Research Funds for the Central Universities, and the Research Funds of Renmin University of China (23XNKJ19); Public Computing Cloud, Renmin University of China.

REFERENCES

- [1] M. M. Bronstein, J. Bruna, T. Cohen, and P. Veličković, “Geometric deep learning: Grids, groups, graphs, geodesics, and gauges,” *arXiv preprint arXiv:2104.13478*, 2021.
- [2] J. Han, J. Cen, L. Wu, Z. Li, X. Kong, R. Jiao, Z. Yu, T. Xu, F. Wu, Z. Wang *et al.*, “A survey of geometric graph neural networks: data structures, models and applications,” *Frontiers of Computer Science*, vol. 19, no. 11, p. 1911375, 2025.
- [3] A. Duval, S. V. Mathis, C. K. Joshi, V. Schmidt, S. Miret, F. D. Malliaros, T. Cohen, P. Lio, Y. Bengio, and M. Bronstein, “A hitchhiker’s guide to geometric gnns for 3d atomic systems,” *arXiv preprint arXiv:2312.07511*, 2023.
- [4] X. Zhang, L. Wang, J. Helwig, Y. Luo, C. Fu, Y. Xie, M. Liu, Y. Lin, Z. Xu, K. Yan, K. Adams, M. Weiler, X. Li, T. Fu, Y. Wang, A. Strasser, H. Yu, Y. Xie, X. Fu, S. Xu, Y. Liu, Y. Du, A. Saxton, H. Ling, H. Lawrence, H. Stärk, S. Gui, C. Edwards, N. Gao, A. Ladera, T. Wu, E. F. Hofgard, A. M. Tehrani, R. Wang, A. Daigavane, M. Bohde, J. Kurtin, Q. Huang, T. Phung, M. Xu, C. K. Joshi, S. V. Mathis, K. Aizzadenesheli, A. Fang, A. Aspuru-Guzik, E. Bekkers, M. Bronstein, M. Zitnik, A. Anandkumar, S. Ermon, P. Liò, R. Yu, S. Günnemann, J. Leskovec, H. Ji, J. Sun, R. Barzilay, T. Jaakkola, C. W. Coley, X. Qian, X. Qian, T. Smidt, and S. Ji, “Artificial intelligence for science in quantum, atomistic, and continuum systems,” *arXiv preprint arXiv:2307.08423*, 2023.
- [5] L. Wu, Z. Hou, J. Yuan, Y. Rong, and W. Huang, “Equivariant spatio-temporal attentive graph networks to simulate physical dynamics,” in *Thirty-seventh Conference on Neural Information Processing Systems*, 2023.
- [6] M. Xu, J. Han, A. Lou, J. Kossaifi, A. Ramanathan, K. Aizzadenesheli, J. Leskovec, S. Ermon, and A. Anandkumar, “Equivariant graph neural operator for modeling 3d dynamics,” in *Forty-first International Conference on Machine Learning*, 2024.
- [7] J. L. Watson, D. Juergens, N. R. Bennett, B. L. Trippe, J. Yim, H. E. Eisenach, W. Ahern, A. J. Borst, R. J. Ragotte, L. F. Milles *et al.*, “De novo design of protein structure and function with rfdiffusion,” *Nature*, vol. 620, no. 7976, pp. 1089–1100, 2023.
- [8] J. B. Ingraham, M. Baranov, Z. Costello, K. W. Barber, W. Wang, A. Ismail, V. Frappier, D. M. Lord, C. Ng-Thow-Hing, E. R. Van Vlack *et al.*, “Illuminating protein space with a programmable generative model,” *Nature*, vol. 623, no. 7989, pp. 1070–1078, Nov 2023.
- [9] V. G. Satorras, E. Hoogeboom, and M. Welling, “E (n) equivariant graph neural networks,” in *International Conference on Machine Learning*. PMLR, 2021, pp. 9323–9332.
- [10] E. Darve, “The fast multipole method: numerical implementation,” *Journal of Computational Physics*, vol. 160, no. 1, pp. 195–240, 2000.
- [11] Y. Zhang, J. Cen, J. Han, Z. Zhang, J. ZHOU, and W. Huang, “Improving equivariant graph neural networks on large geometric graphs via virtual nodes learning,” in *Forty-first International Conference on Machine Learning*, 2024.
- [12] K. M. Borgwardt, A. Gretton, M. J. Rasch, H.-P. Kriegel, B. Schölkopf, and A. J. Smola, “Integrating structured biological data by kernel maximum mean discrepancy,” *Bioinformatics*, vol. 22, no. 14, pp. e49–e57, 2006.
- [13] K. T. Schütt, H. E. Sauceda, P.-J. Kindermans, A. Tkatchenko, and K.-R. Müller, “SchNet—a deep learning architecture for molecules and materials,” *The Journal of Chemical Physics*, vol. 148, no. 24, p. 241722, 2018.
- [14] J. Klicpera, J. Groß, and S. Günnemann, “Directional message passing for molecular graphs,” in *International Conference on Learning Representations*, 2020.
- [15] N. Thomas, T. Smidt, S. Kearnes, L. Yang, L. Li, K. Kohlhoff, and P. Riley, “Tensor field networks: Rotation-and translation-equivariant neural networks for 3d point clouds,” *arXiv preprint arXiv:1802.08219*, 2018.
- [16] J. Brandstetter, R. Hesselink, E. van der Pol, E. J. Bekkers, and M. Welling, “Geometric and physical quantities improve e(3) equivariant message passing,” in *International Conference on Learning Representations*, 2022.
- [17] F. Fuchs, D. Worrall, V. Fischer, and M. Welling, “Se(3)-transformers: 3d roto-translation equivariant attention networks,” in *Annual Conference on Neural Information Processing Systems*, vol. 33, 2020.
- [18] J. Köhler, L. Klein, and F. Noé, “Equivariant flows: sampling configurations for multi-body systems with symmetric energies,” *arXiv preprint arXiv:1910.00753*, 2019.
- [19] B. Jing, S. Eismann, P. Suriana, R. J. L. Townshend, and R. Dror, “Learning from protein structure with geometric vector perceptrons,” in *International Conference on Learning Representations*, 2021.
- [20] J. Cen, A. Li, N. Lin, Y. Ren, Z. Wang, and W. Huang, “Are high-degree representations really unnecessary in equivariant graph neural networks?” in *Annual Conference on Neural Information Processing Systems*, 2024.
- [21] J. Gilmer, S. S. Schoenholz, P. F. Riley, O. Vinyals, and G. E. Dahl, “Neural message passing for quantum chemistry,” in *International Conference on Machine Learning*, 2017.
- [22] T. Pham, T. Tran, H. Dam, and S. Venkatesh, “Graph classification via deep learning with virtual nodes,” *arXiv preprint arXiv:1708.04357*, 2017.
- [23] E. Hwang, V. Thost, S. S. Dasgupta, and T. Ma, “An analysis of virtual nodes in graph neural networks for link prediction,” in *The First Learning on Graphs Conference*, 2022.
- [24] J. Han, W. Huang, H. Ma, J. Li, J. B. Tenenbaum, and C. Gan, “Learning physical dynamics with subequivariant graph neural networks,” in *Advances in Neural Information Processing Systems*, 2022.
- [25] X. Kong, W. Huang, and Y. Liu, “Conditional antibody design as 3d equivariant graph translation,” in *The Eleventh International Conference on Learning Representations*, 2023.
- [26] H. Ma, Y. Rong, and J. Huang, “Graph neural networks: Scalability,” *Graph Neural Networks: Foundations, Frontiers, and Applications*, pp. 99–119, 2022.
- [27] H. Ding, Z. Wei, and Y. Ye, “Scalable and effective graph neural networks via trainable random walk sampling,” *IEEE Transactions on Knowledge and Data Engineering*, vol. 37, no. 2, pp. 896–909, 2025.
- [28] V. Md, S. Misra, G. Ma, R. Mohanty, E. Georganas, A. Heinecke, D. Kalamkar, N. K. Ahmed, and S. Avancha, “Distgcn: Scalable distributed training for large-scale graph neural networks,” in *Proceedings of the International Conference for High Performance Computing, Networking, Storage and Analysis*, 2021, pp. 1–14.
- [29] W. Huang, J. Han, Y. Rong, T. Xu, F. Sun, and J. Huang, “Equivariant graph mechanics networks with constraints,” in *International Conference on Learning Representations*, 2022.
- [30] S. Villar, D. W. Hogg, K. Storey-Fisher, W. Yao, and B. Blum-Smith, “Scalars are universal: Equivariant machine learning, structured like classical physics,” in *Annual Conference on Neural Information Processing Systems*, 2021.
- [31] G. Karypis and V. Kumar, “Metis—a software package for partitioning unstructured graphs, partitioning meshes and computing fill-reducing ordering of sparse matrices,” 01 1997.
- [32] T. Kipf, E. Fetaya, K.-C. Wang, M. Welling, and R. Zemel, “Neural relational inference for interacting systems,” in *International Conference on Machine Learning*, 2018.
- [33] J. Han, W. Huang, T. Xu, and Y. Rong, “Equivariant graph hierarchy-based neural networks,” in *Annual Conference on Neural Information Processing Systems*, 2022.
- [34] Richard J. Gowers, Max Linke, Jonathan Barnoud, Tyler J. E. Reddy, Manuel N. Melo, Sean L. Seyler, Jan Domański, David L. Dotson, Sébastien Buchoux, Ian M. Kenney, and Oliver Beckstein, “MDAnalysis: A Python Package for the Rapid Analysis of Molecular Dynamics Simulations,” in *Proceedings*

- of the 15th Python in Science Conference*, Sebastian Benthall and Scott Rostrup, Eds., 2016, pp. 98 – 105.
- [35] S. Seyler and O. Beckstein, “Molecular dynamics trajectory for benchmarking mdanalysis,” p. m9, 2017.
 - [36] A. Sanchez-Gonzalez, J. Godwin, T. Pfaff, R. Ying, J. Leskovec, and P. Battaglia, “Learning to simulate complex physics with graph networks,” in *International Conference on Machine Learning*. PMLR, 2020, pp. 8459–8468.
 - [37] B. Ummenhofer, L. Prantl, N. Thuerey, and V. Koltun, “Lagrangian fluid simulation with continuous convolutions,” in *International Conference on Learning Representations*, 2020.
 - [38] J. Bender *et al.*, “SPlisHSPlasH Library.” [Online]. Available: <https://github.com/InteractiveComputerGraphics/SPlisHSPlasH>

APPENDIX

A. Proof

Theorem A.1 (Proposition IV.1). *If the initialization of the virtual nodes satisfies Eq. (2), then after Eqs. (3) to (9), the output coordinates $\vec{X}^{(L)}$ are E(3)-equivariant and permutation-equivariant, the virtual coordinates $\vec{Z}^{(L)}$ are E(3)-equivariant and permutation-invariant, with respect to the input $\vec{X}^{(0)}$.*

Proof. Consider a sequence composed of functions $\{\phi_i : \mathcal{X}^{(i-1)} \rightarrow \mathcal{X}^{(i)}\}_{i=1}^N$ equivariant to a same group G , the equivariance lead to an interesting property that

$$\phi_N \circ \dots \circ \phi_{i+1} \circ \rho_{\mathcal{X}^{(i)}}(g) \phi_i \circ \dots \circ \phi_1 = \phi_N \circ \dots \circ \phi_{j+1} \circ \rho_{\mathcal{X}^{(j)}}(g) \phi_j \circ \dots \circ \phi_1,$$

holds for all $i, j = 1, 2, \dots, N$ and $g \in G$, which means that the group elements g can be freely exchanged in the composite sequence of equivariant functions. In particular, if one of the equivariant functions (e.g. ϕ_k) is replaced by an invariant function, the group element g will be absorbed, that means

$$\phi_N \circ \dots \circ \phi_k \circ \dots \circ \phi_{i+1} \circ \rho_{\mathcal{X}^{(i)}}(g) \phi_i \circ \dots \circ \phi_1 = \phi_N \circ \dots \circ \phi_1.$$

holds for all $g \in G$ but only $i = 1, 2, \dots, k$. Although $\phi_N \circ \dots \circ \phi_k$ is still equivariant, because the group elements must be input starting from ϕ_1 , the overall $\phi_N \circ \dots \circ \phi_1$ is still an invariant function.

Since Eq. (2) is the definition of a function with E(3)-equivariance and permutation-invariance, and the pooling operators like sum or mean maintain permutation-equivariance of the whole model. Now to prove the E(3)-equivariance of the whole model, we choose to give a stronger conclusion, namely each of Eqs. (3) to (5), (7) and (9) is an E(3)-invariant function, and each of Eqs. (6) and (8) is an E(3)-equivariant function.

It is obvious that each input in Eqs. (3) to (5), (7) and (9) is either a constant or an inner product term, thus ensuring the E(3)-invariance of each function. And each of Eqs. (6) and (8) is linear combination of three-dimensional vectors with an E(3)-invariant weight, thus ensuring the E(3)-equivariance of each function. \square

Theorem A.2. *The E(3)-equivariant function $f(\vec{x}_i, \vec{Z})$ in Proposition IV.3 can be decomposed into an O(3)-equivariant and translation-invariant function of $\vec{Z} - \vec{x}_i$, and the addition of \vec{x}_i .*

Proof. Since $f(\vec{x}_i, \vec{Z})$ is equivariant to translation \vec{t} , considering $\vec{t} = -\vec{x}_i$, we get

$$f(\vec{x}_i, \vec{Z}) = f(\vec{x}_i, \vec{Z}) - \vec{x}_i + \vec{x}_i = f(\vec{x}_i - \vec{x}_i, \vec{Z} - \vec{x}_i) + \vec{x}_i = f(\vec{0}, \vec{Z} - \vec{x}_i) + \vec{x}_i := h(\vec{Z} - \vec{x}_i) + \vec{x}_i. \quad \square$$

Lemma A.3. *For any O(3)-equivariant function $\hat{f}(\vec{Z})$, it must fall into the subspace spanned by the columns of \vec{Z} , namely, there exists a function $s(\vec{Z})$, satisfying $\hat{f}(\vec{Z}) = \vec{Z}s(\vec{Z})$.*

Proof. The proof is given by [30]. Essentially, suppose \vec{Z}^\perp is the orthogonal complement of the column space of \vec{Z} . Then there must exist functions $s(\vec{Z})$ and $s^\perp(\vec{Z})$, satisfying $\hat{f}(\vec{Z}) = \vec{Z}s(\vec{Z}) + \vec{Z}^\perp s^\perp(\vec{Z})$. We can always find an orthogonal transformation O allowing $O\vec{Z} = \vec{Z}$ while $O\vec{Z}^\perp = -\vec{Z}^\perp$. With this transformation O , we have $\hat{f}(O\vec{Z}) = \hat{f}(\vec{Z}) = \vec{Z}s(\vec{Z}) + \vec{Z}^\perp s^\perp(\vec{Z})$, and $O\hat{f}(\vec{Z}) = \vec{Z}s(\vec{Z}) - \vec{Z}^\perp s^\perp(\vec{Z})$. The equivariance property of \hat{f} implies $\vec{Z}s(\vec{Z}) + \vec{Z}^\perp s^\perp(\vec{Z}) = \vec{Z}s(\vec{Z}) - \vec{Z}^\perp s^\perp(\vec{Z})$, which derives $s^\perp(\vec{Z}) = 0$. Hence, the proof is concluded. \square

Lemma A.4. *If the O(3)-equivariant function $\hat{f}(\vec{Z})$ lies in the subspace spanned by the columns of \vec{Z} , then there exists a function σ satisfying $\hat{f}(\vec{Z}) = \vec{Z}\sigma(\vec{Z}^\top \vec{Z})$.*

Proof. The proof is provided by Corollary 2 in [29]. The basic idea is that $\hat{f}(\vec{Z})$ can be transformed to $\hat{f}(\vec{Z}) = \vec{Z}\eta(\vec{Z})$ where $\eta(\vec{Z})$ is O(3)-invariant. According to Lemma 1-2 in [29], $\eta(\vec{Z})$ must be written as $\eta(\vec{Z}) = \sigma(\vec{Z}^\top \vec{Z})$, which completes the proof. \square

Theorem A.5. *There exists a surjection from dao to $(\vec{Z} - \vec{x}_i)^\top (\vec{Z} - \vec{x}_i)$, that is*

$$\exists \text{ a function } \zeta, \quad (\vec{Z} - \vec{x}_i)^\top (\vec{Z} - \vec{x}_i) = \zeta \left(\bigoplus_{c=1}^C \|\vec{z}_c - \vec{x}_i\|^2, (\vec{Z} - \vec{x}_i)^\top (\vec{Z} - \vec{x}_i) \right).$$

Proof. First, we simplify the notation as

$$\mathbf{A} := (\vec{Z} - \vec{x}_i)^\top (\vec{Z} - \vec{x}_i), \quad \mathbf{D} := (\vec{Z} - \vec{x}_i)^\top (\vec{Z} - \vec{x}_i), \quad \mathbf{Y} := \bigoplus_{c=1}^C \|\vec{z}_c - \vec{x}_i\|^2.$$

Since $\vec{Z} - \vec{x}_i = (\vec{Z} - \vec{x}) - (\vec{x}_i - \vec{x})$, letting $\vec{Z}' = \vec{Z} - \vec{x}$, $\vec{x}' = \vec{x}_i - \vec{x}$, $\vec{z}'_c = \vec{z}'_{:,c}$, we have

$$\mathbf{A} = (\vec{Z}' - \vec{x}')^\top (\vec{Z}' - \vec{x}'), \quad \mathbf{D} = \vec{Z}'^\top \vec{Z}', \quad \mathbf{Y} = \bigoplus_{c=1}^C \|\vec{z}'_c - \vec{x}'\|^2.$$

Thus, we find the following equations:

$$\begin{aligned}
\mathbf{A}_{mn} &= \langle \vec{z}'_m - \vec{x}', \vec{z}'_n - \vec{x}' \rangle \\
&= \langle \vec{z}'_m, \vec{z}'_n \rangle + \frac{1}{2} (\langle \vec{x}', \vec{x}' - 2\vec{z}'_m \rangle + \langle \vec{x}', \vec{x}' - 2\vec{z}'_n \rangle) \\
&= \langle \vec{z}'_m, \vec{z}'_n \rangle + \frac{1}{2} ((\|\vec{z}'_m - \vec{x}'\|^2 - \|\vec{z}'_m\|^2) + (\|\vec{z}'_n - \vec{x}'\|^2 - \|\vec{z}'_n\|^2)) \\
&= \mathbf{D}_{mn} + \frac{1}{2} ((\mathbf{Y}_m - \mathbf{D}_{mm}) + (\mathbf{Y}_n - \mathbf{D}_{nn})),
\end{aligned}$$

and

$$\begin{aligned}
\mathbf{Y}_m &= \mathbf{A}_{mm}, \\
\mathbf{D}_{mn} &= \mathbf{A}_{mn} - \frac{1}{2}(\mathbf{A}_{mm} + \mathbf{A}_{nn}) + \frac{1}{2}(\mathbf{D}_{mm} + \mathbf{D}_{nn}),
\end{aligned}$$

which means there is a surjection from $\bigoplus_{c=1}^C \|\vec{z}_c - \vec{x}_i\|^2, (\vec{Z} - \vec{x})^\top (\vec{Z} - \vec{x})$ to $(\vec{Z} - \vec{x}_i)^\top (\vec{Z} - \vec{x}_i)$. \square

Theorem A.6 (Proposition IV.3). *The update function must take the form $f(\vec{x}_i, \vec{Z}) = \vec{x}_i + \sum_{c=1}^C (\vec{z}_c - \vec{x}_i) \psi_c \left(\bigoplus_{c=1}^C \|\vec{z}_c - \vec{x}_i\|^2, \mathbf{m}^v \right)$, where $\psi_c : \mathbb{R}^{C+C^2} \rightarrow \mathbb{R}$ is an arbitrary non-linear function, and \mathbf{m}^v is an $E(3)$ -invariant term by Eq. (5).*

Proof. According to Theorem A.2, there exists an $O(3)$ -equivariant and transform-invariant function h , thus

$$f(\vec{x}_i, \vec{Z}) = h(\vec{Z} - \vec{x}_i) + \vec{x}_i.$$

Then, from Lemma A.4, we rewrite the $O(3)$ -equivariant h into a product of the vector $\vec{Z} - \vec{x}_i$ and a scalar function η with an inner-product input, that is,

$$f(\vec{x}_i, \vec{Z}) = (\vec{Z} - \vec{x}_i) \eta \left((\vec{Z} - \vec{x}_i)^\top (\vec{Z} - \vec{x}_i) \right) + \vec{x}_i.$$

Finally, with Theorem A.5, we transform it into a more expressive function as

$$f(\vec{x}_i, \vec{Z}) = (\vec{Z} - \vec{x}_i) \psi \left(\bigoplus_{c=1}^C \|\vec{z}_c - \vec{x}_i\|^2, (\vec{Z} - \vec{x})^\top (\vec{Z} - \vec{x}) \right) + \vec{x}_i,$$

which is equivalent to Eq. (5). \square

B. Experiment Details

1) Dataset Details

TABLE VIII

BASIC STATISTICS OF THE FOUR DATASETS, WITH GRAPH SIZES INCREASING PROGRESSIVELY. AMONG THEM, FLUID113K IS OUR GENERATED LARGE-SCALE FLUID SIMULATION DATASET, WHERE EACH GRAPH CONTAINS OVER 100K NODES AND AN AVERAGE OF 1.7M EDGES.

	N -body System	Protein Dynamics	Water-3D	Fluid113K
Number of Samples (Train / Valid / Test)	5,000/2,000/2,000	2,481/827/863	15,000/1,500/1,500	1,600/320/320
Number of Nodes (N)	100	855	7,806 (Avg)	113,140 (Avg)
Number of Edges ($ \mathcal{E} $)	9,900	55,107 (Avg)	94,931 (Avg)	1,706,973 (Avg)
Default Radius (r)	∞	10Å	0.035	0.075
Predict Time Interval (Δt)	10	15	15	20

2) Implementation Details

TABLE IX

DEFAULT HYPER-PARAMETERS ON FOUR DATASETS

Hyperparameter	N -body System	Protein Dynamics	Water-3D	Fluid-113K
Bandwidth σ in Eq. (10)	1.5	1.0	1.5	3.0
Balancing factor λ in Eq. (11)	0.03	0.50	0.01	0.01
Number of Sampled Nodes N in Eq. (10)	3	3	3	50
Number of Virtual Channel C	{1, 3, 10}	{1, 3, 10}	{1, 3, 10}	{5}
Learning Rate	5e-4	5e-4	5e-4	5e-4
Weight Decay	1e-12	1e-12	1e-12	1e-12
Epochs	2500	2000	2000	2500
Early Stop	200	100	100	100
Number of Layers	4	4	4	4
Hidden Dimension	64	64	64	64